Lithos 245 (2016) 223–242

Contents lists available at ScienceDirect

Lithos

journal homepage: www.elsevier.com/locate/lithos

Underplating of basaltic magmas and crustal growth in a continental arc: Evidence from Late Mesozoic intermediate–felsic intrusive rocks in southern Qiangtang, central Tibet

Lu-Lu Hao [a,b], Qiang Wang [a,c,*], Derek A. Wyman [d], Quan Ou [a,b], Wei Dan [a], Zi-Qi Jiang [a,e], Fu-Yuan Wu [f], Jin-Hui Yang [f], Xiao-Ping Long [a], Jie Li [a]

[a] State Key Laboratory of Isotope Geochemistry, Guangzhou Institute of Geochemistry, Chinese Academy of Sciences, Guangzhou 510640, China
[b] University of Chinese Academy of Sciences, Beijing 10069, China
[c] CAS Center for Excellence in Tibetan Plateau Earth Sciences, China
[d] School of Geosciences, The University of Sydney, NSW 2006, Australia
[e] School of Earth Science, Guilin University of Technology, Guilin 541004, China
[f] Institute of Geology and Geophysics, Chinese Academy of Science, Beijing 100029, China

ARTICLE INFO

Article history:
Received 8 April 2015
Accepted 16 September 2015
Available online 28 September 2015

Keywords:
Crustal growth
Underplating
Adakites
Late Mesozoic
Qiangtang
Tibet

ABSTRACT

Phanerozoic growth of continental crust has widely been considered as an important geological phenomenon and mainly occurs in an arc setting. However, the crustal growth models (mantle-derived basalt underplating or accretion of island or intra-oceanic arc complexes or oceanic plateau) have been disputed. Here we present new zircon LA–ICPMS U–Pb age, whole-rock major and trace element, Sr–Nd and zircon Hf isotopic data for Late Mesozoic intermediate–felsic intrusive rocks in the Rena Co area in southern Qiangtang, central Tibet. LA–ICP–MS zircon U–Pb dating for two granodiorite and three diorite samples and one granodiorite porphyry sample gives ages of ca. 150 Ma, ca. 112 Ma, respectively, indicating they were generated in the Late Jurassic–Early Cretaceous. All rocks are sub-alkaline in composition and belong to the high-K cal-alkaline series. The ~150 Ma diorites (SiO_2 = 57.9–61.2 wt.%) exhibit relatively high MgO (3.13–3.88 wt.%) and Cr (52.4–282 ppm) contents and $Mg^{\#}$ (47–51) values, similar to magnesian diorites. They are geochemically characterized by uniformly low $\varepsilon_{Nd}(t)$ (−5.5 to −5.2), high $(^{87}Sr/^{86}Sr)_i$ (0.7071 to 0.7078) and Th/La (0.22–0.32), and variable zircon $\varepsilon_{Hf}(t)$ (−8.7 to +4.8) values. They were probably generated by melting of oceanic sediment diapirs, followed by interaction with the surrounding mantle during the northward subduction of Bangong–Nujiang Oceanic lithosphere. The ~150 Ma granodiorites and ~112 Ma granodiorite porphyries are characterized by low MgO (<3 wt.%) contents and $Mg^{\#}$ (<45) values, high Al_2O_3 (>15% wt.%) and Sr (>400 ppm) and low Y (<18 ppm) and Yb (<1.9 ppm) contents, and high Sr/Y and La/Yb ratios, which are similar to those of typical adakites. The granodiorites have low $\varepsilon_{Nd}(t)$ (−7.6 to −3.7) and zircon $\varepsilon_{Hf}(t)$ (−9.8 to +0.2) and high $(^{87}Sr/^{86}Sr)_i$ (0.7069 to 0.7086) values, and were likely produced by partial melting of a thickened and heterogeneous ancient lower continental crust. The relatively depleted isotope compositions [$(^{87}Sr/^{86}Sr)_i$ = 0.7054–0.7065; $\varepsilon_{Nd}(t)$ = −0.61 to +0.25; zircon $\varepsilon_{Hf}(t)$ = +4.7 to +9.7] of the granodiorite porphyries indicate that they were most probably generated by partial melting of newly underplated and thickened basaltic lower crust. Taking into account ophiolites in the Bangong–Nujiang Suture and Late Mesozoic magmatic rocks in the southern Qiangtang sub-block, we suggest that this area was located in a continental arc setting. Moreover, from the Late Jurassic to Early Cretaceous, the ancient lower crust in the southern Qiangtang sub-block was gradually replaced by mantle-derived juvenile materials. The crustal evolution indicates that, in a continental arc, basaltic magma underplating plays a key role in vertical crustal growth.

1. Introduction

One of the Earth's unique features when compared with other planets in our Solar System is the presence of the continental crust (Rudnick, 1995). However, the growth and evolution of the continental crust remains the topic of considerable debate (e.g., Hawkesworth and Kemp, 2006; Jahn, 2004). It is widely accepted that the formation of

* Corresponding author at: Key Laboratory of Isotope Geochronology and Geochemistry, Guangzhou Institute of Geochemistry, Chinese Academy of Sciences, Guangzhou 510640, China.
E-mail address: wqiang@gig.ac.cn (Q. Wang).

http://dx.doi.org/10.1016/j.lithos.2015.09.015
0024-4937/

the continental crust was essentially complete in the Precambrian (Condie, 1998; Taylor and McLennan, 1995). However, in recent decades, this idea was challenged by isotope investigations in western North America (Sierra Nevada, Peninsular Range, and Canadian Cordillera) (Lee et al., 2007; Samson et al., 1989), South America (Andean) (Mišković and Schaltegger, 2009), eastern Australia (Lachlan and New England Fold belts) (Collins, 1998; McCulloch and Chappell, 1982), the central Asian Orogenic Belt (also known as the Altaid Tectonic Collage) (e.g., Jahn, 2004; Kröner et al., 2014; Sengör et al., 1993) and south Tibet (Gangdese belt) (e.g., Chu et al., 2006; Ji et al., 2009; Ma et al., 2013a; Mo et al., 2008; Zhang et al., 2014c; Zhu et al., 2011), which revealed that a substantial proportion of Phanerozoic crust is juvenile. Phanerozoic continental crustal growth primarily occurs in subduction zones by lateral accretion of island or intra-oceanic arc complexes and oceanic plateaus or by vertical addition by underplating of basaltic magmas in the crust–mantle interface (Chen and Arakawa, 2005; Jahn, 2004; Rudnick, 1995).

Numerous studies in southern Tibet indicate that Jurassic–Early Eocene Gangdese granitoids with high and positive εNd(t) have important implications for Gangdese crustal growth (e.g., Chu et al., 2006; Ji et al., 2009; Ma et al., 2013a; Zhang et al., 2014c). Geochemical investigations of Early Cretaceous igneous rocks along an east–west traverse in central and northern Lhasa sub-block reveal basalt underplating-related vertical crustal growth, plausibly triggered by break-off in a continent–continent collision setting in central Tibet (e.g., Sui et al., 2013; Zhu et al., 2009, 2011). Recently, however, Zhang et al. (2014a) reported the occurrence of a Meso-Tethyan oceanicplateau in the Bangong–Nujiang Ocean, in the Late Mesozoic (193–173 Ma and 128–104 Ma), indicating lateral crustal growth by accretion of oceanic plateau. Therefore, we suggest that the mechanism and tectonic setting for Late Mesozoic crustal growth in central Tibet remains unclear.

Granitoids are the main components of continental crust. Much work has been done on their Sr–Nd isotopic compositions to better understand their genesis and thus the origin and evolution of the continental crust (e.g., Jahn, 2004). Phanerozoic granitoids that originated from juvenile crust have rather different initial Sr–Nd isotopic compositions compared to those derived from ancient crust because juvenile crust (middle oceanic ridge basalt (MORB), oceanic island basalt (OIB), and newly underplated basalts) have positive $\varepsilon_{Nd}(t)$ and low $(^{87}Sr/^{86}Sr)_i$, while old continental crustal rocks generally have negative $\varepsilon_{Nd}(t)$ and high $(^{87}Sr/^{86}Sr)_i$ (e.g., Chen and Arakawa, 2005). Recently, Hf isotope analyses on zircons have been widely used to trace the source regions of their host magmas. Due to the mineral's physiochemical resistance, the isotopic data can readily distinguish the involvement of newly derived mantle melts from the remelting of old mature crust (Griffin et al., 2002; Kemp et al., 2007; Yang et al., 2007; Zhu et al., 2011).

Mesozoic intermediate–felsic intrusive rocks are widely distributed in the southern Qiangtang, central Tibet (e.g., Kapp et al., 2005; Li et al., 2014a). In this study, we report zircon LA–ICPMS U–Pb age, whole-rock major and trace element, Sr–Nd and zircon Hf isotopic data for Late Jurassic granodiorites and diorites and Early Cretaceous granodiorite porphyries in the Rena Co area, north of Gerze County in southern Qiangtang. We systematically investigate their petrogenesis and tectonic setting and trace the temporal variations of their source regions, with important implications for crustal growth in central Tibet.

2. Geological setting and petrographical characteristics

The Tibetan plateau consists of five blocks (from north to south: Qaidam, Songpan–Ganze–Hoh Xil, Qiangtang, Lhasa, and Himalaya), mainly separated by four sutures (Anyimaqin–Kunlun–Muztagh, Jinsha, Bangong–Nujiang and Indus–Yalu Sutures, respectively. Fig. 1a) (Chung et al., 2005; Yin and Harrison, 2000). The Qiangtang block is located in central Tibet, and is bounded by the Jinsha Suture (JS) to the north and the Bangong–Nujiang Suture (BNS) to the south (Yin and Harrison, 2000). It is divided into southern and northern Qiangtang sub-blocks by Longmu–Shuanghu suture (Li et al., 2006; Pan et al., 2004).

The Bangong–Nujiang Suture Zone (BNSZ), which extends over 2000 km across central Tibet, is characterized by mainly Jurassic–Cretaceous flysch, mélange and scattered ophiolitic fragments representing remnants of the Bangong–Nujiang ocean basin (Kapp et al., 2003; Pan et al., 2004). The main strata exposed in southern Qiangtang sub-block consist of Carboniferous and Permian interbedded sandstone and shale, Triassic limestone, and Jurassic sandstone (Pan et al., 2004) (Fig. 1c). Late Mesozoic magmatic rocks are widely distributed in the southern Qiangtang from the Rotug to Amdo area (Fig. 1b). These rocks are dominated by intermediate–felsic magmatic rocks and currently available geochronological data (e.g., Chang et al., 2011; Guynn et al., 2006; Kapp et al., 2005; Li et al., 2011, 2013, 2014a,b; Liu et al., 2012, 2014; Zhang et al., 2012a) indicate that they were emplaced between 183 and 101 Ma.

The Rena Co (lake) area, approximately 40 km north of Gerze County, is located in the southern Qiangtang sub-block (Fig. 1b) and includes five unnamed intermediate-felsic plutons. As numbered in Fig. 2, plutons ① and ②, ③ and ④, and ⑤ consist of granodiorites, diorites and granodiorite porphyries, respectively.

Granodiorites contain amphibole (5–10 vol.%), biotite (10–15 vol.%), plagioclase (60–65 vol.%), and quartz (10–15 vol.%) with accessory zircon, apatite and Fe–Ti oxides (Fig. 2a–d). Diorites contain amphibole (10–15 vol.%), biotite (20–25 vol.%), plagioclase (55–60 vol.%), and quartz (~5 vol.%) with accessory zircon, apatite, titanite, and Fe–Ti oxides (Fig. 2e–h). Granodiorite porphyries are typically porphyritic, with 40–50 vol.% phenocrysts of plagioclase, biotite and quartz and matrix composed mainly of K-feldspar and quartz (Fig. 2i–j).

3. Analytical methods

The samples used for geochemical analyses were powdered to ~200-mesh size in an agate mortar. Major element oxides were analyzed on fused glass beads using a Rigaku RIX 2000 X-ray fluorescence spectrometer at the State Key Laboratory of Isotope Geochemistry, Guangzhou Institute of Geochemistry, Chinese Academy of Sciences (SKLaBIG, GIGCAS). Calibration lines used in quantification were produced by bivariate regression of data from 36 reference materials encompassing a wide range of silicate compositions (Li et al., 2004). Analytical uncertainties are between 1% and 5%. Trace elements were analyzed using an Agilent 7500a ICP–MS at GIGCAS. Analytical procedures were similar to those described by Li et al. (2004). A set of USGS and Chinese national rock standards, including BHVO-2, GSR-1, GSR-2, GSR-3, AGV-2, W-2 and SARM-4 were chosen for calibration. Analytical precision typically is better than 5%. The major and trace element data are listed in Table 1.

Sr and Nd isotope analyses were performed using a Micromass Isoprobe multi-collector mass spectrometer (MC–ICPMS) at SKLaBIG, GIGCAS. Analytical procedures are described by Li et al. (2004). The $^{87}Sr/^{86}Sr$ ratio of the NBS987 standard and $^{143}Nd/^{144}Nd$ ratio of the Shin Etsu JNdi-1 standard measured were 0.710251 ± 6 ($n = 19$, 2σ) and 0.512087 ± 3 ($n = 11$, 2σ), respectively. All measured $^{143}Nd/^{144}Nd$ and $^{86}Sr/^{88}Sr$ ratios are fractionation corrected to $^{146}Nd/^{144}Nd = 0.7219$ and $^{86}Sr/^{88}Sr = 0.1194$, respectively. The Sr–Nd isotope data are presented in Table 1.

Zircon crystals were separated from six rock samples using standard density and magnetic separation techniques. Zircon grains were handpicked and mounted in an epoxy resin disk, and then polished and coated with gold. Cathodoluminescence (CL) images were taken at SKLaBIG, GIGCAS with a JEOL JXA-8100 Superprobe for inspecting

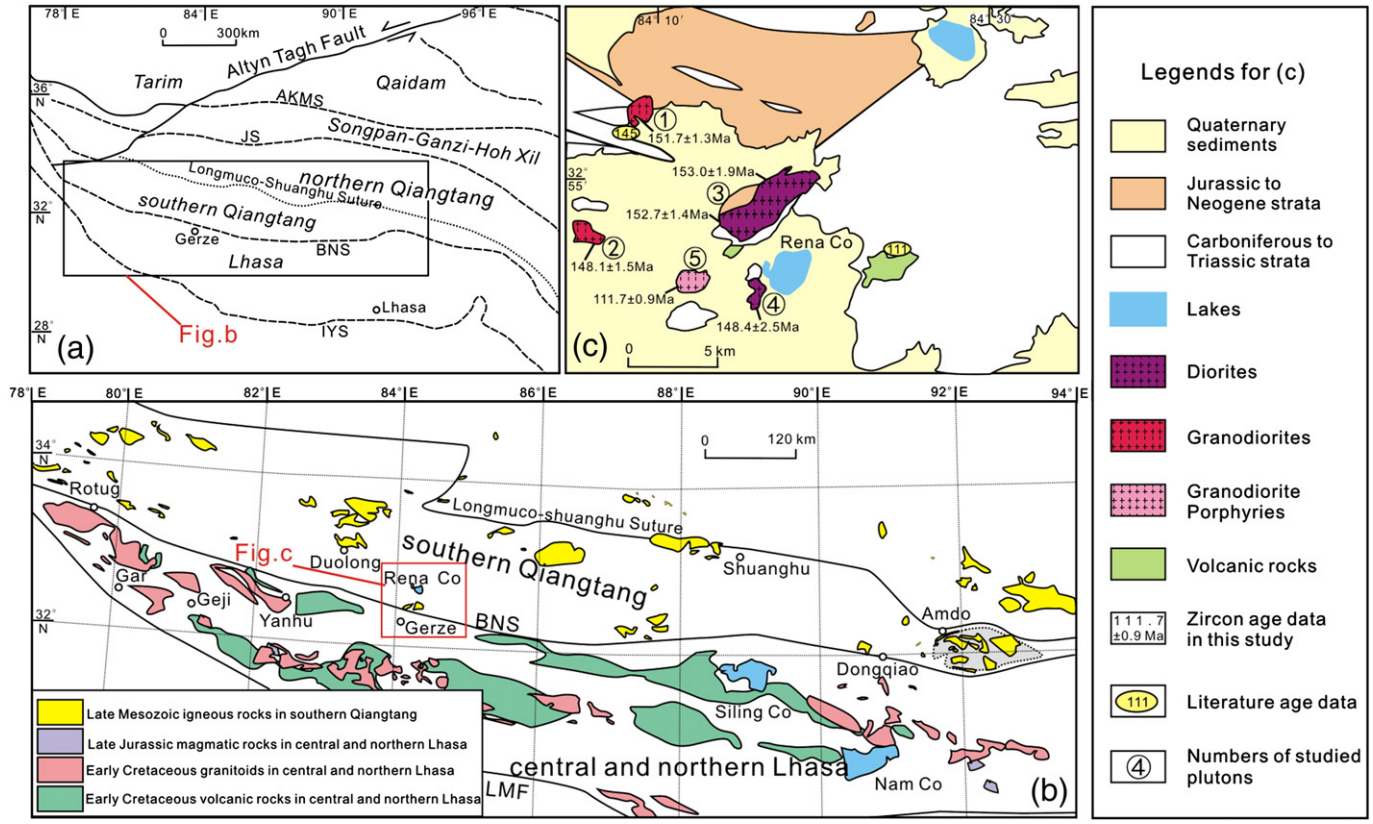

Fig. 1. (a) Tectonic framework of the Tibetan Plateau (modified from diagrams of Chung et al. (2005) and Yin and Harrison (2000)). Main suture zones between major blocks: AKMS, Ayimaqen–Kunlun–Mutztagh suture; JS, Jinsha suture; BNS, Bangong–Nujiang suture; and IYS, Indus–Yalu suture. (b) Map of the central Tibetan Plateau showing the distribution of Late Mesozoic igneous rocks in southern Qiangtang and central and northern Lhasa sub-blocks. LMF, Luobadui–Milanshan Fault. (c) Simplified geologic map showing outcrops of magmatic rocks in the Rena Co area, southern Qiangtang, central Tibet. Literature age data are from Kapp et al. (2005) and Chang et al. (2011).

internal morphology of individual zircons and for selecting positions for U–Pb age and Lu–Hf isotope analyses.

Zircon U–Pb dating was conducted at the MC–ICPMS laboratory of the Institute of Geology and Geophysics, Chinese Academy of Sciences (IGGCAS) in Beijing, China. Detailed operating conditions for the laser ablation system and the ICP–MS instrument and data reduction were the same as those described in Xie et al. (2008). An Agilent 7500a quadruple (Q)–ICPMS and a Neptune multi-collector (MC)–ICPMS with a 193 nm excimer ArF laser-ablation system (GeoLas Plus) attached were used for simultaneous determination of zircon U–Pb ages. Uncertainties on individual analyses in the data tables are reported at a 1σ level. Mean ages for pooled U/Pb and Pb/Pb analyses are quoted with 2σ and/or 95% confidence intervals. $^{207}Pb/^{206}Pb$ and $^{206}Pb/^{238}U$ ratios were calculated using the ICPMSDataCal software (Liu et al., 2009), using the zircon standard 91500 as an external standard. Common Pb was corrected according to the method proposed by Andersen (2002). The weighted mean U–Pb ages and concordia plots were processed using the Isoplot/Ex v.3.0 program (Ludwig, 2003). LA–ICP–MS zircon U–Pb isotopic data are presented in the Supplementary Data.

In situ Hf isotope measurements were subsequently undertaken using LA–ICPMS with a beam size of 60 μm and laser pulse frequency of 8 Hz at the MC–ICPMS laboratory of IGGCAS. Lu–Hf isotopic analyses were conducted on the same zircons that were previously analyzed for U–Pb isotopes. Details of instrumental conditions and data acquisition were given in Wu et al. (2006). Our determined $^{176}Hf/^{177}Hf$ ratios for zircon standards MUD (0.282504 ± 0.000002) and GJ-1 (0.282018 ± 0.000004) were in good agreement within errors with the reported values (e.g., Wu et al., 2006). Zircon Hf isotopic data are listed in the Supplementary Data.

4. Results

4.1. Zircon U–Pb dating results

Zircons from six samples including three diorite samples, two granodiorite samples and one granodiorite porphyry sample are mostly euhedral to subhedral, with lengths of 80–250 μm, and length to width ratios of 1:1 to 4:1 (Fig. 3). Most grains show oscillatory zoning (Fig. 3), which is characteristic of igneous zircons (Belousova et al., 2002). Zircon U–Pb age data for six samples are shown in Fig. 3.

Eighteen and twenty-one zircon U–Pb analyses for diorite samples 13GZ09-1 and 13GZ11-1 yield weighted mean $^{206}Pb/^{238}U$ ages of 153.0 ± 1.9 Ma, 152.7 ± 1.4 Ma, respectively (Fig. 3a–b). Nine analyses for one diorite sample 13GZ15-1 are concordant and give a weighted mean $^{206}Pb/^{238}U$ age of 148.4 ± 2.5 Ma and the remaining five analyses produce slightly younger and discordant ages (Fig. 3c) due to significant radiogenic Pb loss probably caused by the later tectono-thermal events. Nineteen analyses for a granodiorite sample 13GZ03 yield a weighted mean $^{206}Pb/^{238}U$ age of 151.7 ± 1.3 Ma (Fig. 3d). In Fig. 3e, three zircons of the granodiorite sample 13GZ25 exhibit variable $^{207}Pb/^{235}U$ ages so that they deviate from the concordia curve (Fig. 3e). This is most likely due to inaccurate radiogenic ^{207}Pb measurements because of its low concentration in these zircons (e.g., Ma et al., 2013a). However, their $^{206}Pb/^{238}U$ ages are nearly concordant with a weighted mean age of 148.1 ± 1.5 Ma that could represent the emplacement age. Twenty-one analyses of one granodiorite porphyry sample (13GZ20-1) yield a weighted mean $^{206}Pb/^{238}U$ age of 111.7 ± 0.9 Ma (Fig. 3f), apart from one spot that shows an inherited age of 145 Ma.

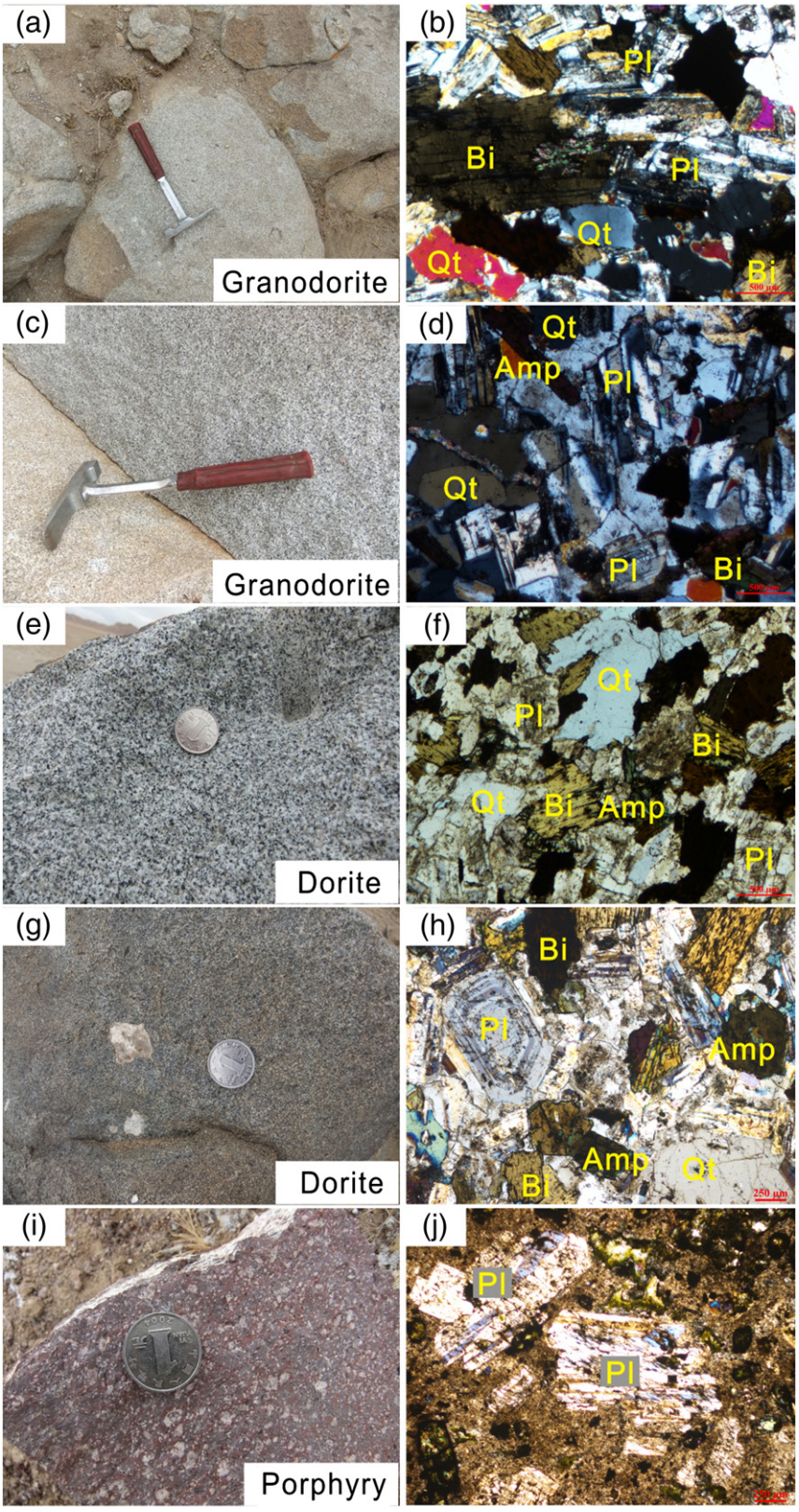

Fig. 2. Field photos (left) and corresponding thin section photomicrographs (right) of the Rena Co intrusive rocks. (a–b) the granodiorite from the pluton ①. (c–d) the granodiorite from the pluton ②. (e–f) the diorite from the pluton ③. (g–h) the diorite from the pluton ④. (i–j) the granodiorite porphyry from the pluton ⑤. Abbreviations: Pl = plagioclase. Amp = amphibole, Kfs = K-feldspar, Bi = biotite, and Qt = quartz.

In summary, (1) the granodiorites and diorites were generated in the Late Jurassic (ca. 150 Ma), with ages similar to those obtained for (~145–160 Ma) intrusive rocks near the Rena Co area by the single zircon U–Pb ion microprobe and ^{40}Ar–^{39}Ar dating (Kapp et al., 2005); (2) the granodiorite porphyries were formed in the late Early Cretaceous (ca. 112 Ma), similar to volcanic rocks in the Rena Co area (Chang et al., 2011; Kapp et al., 2005).

4.2. Major and trace elements

The studied samples include diorites, granodiorites and granodiorite porphyries (Fig. 4a), all of which plot within the high-K cal-alkine field on the diagram of K_2O versus SiO_2 (Fig. 4b).

The Rena Co diorites have SiO_2 ranging from 57.9 to 61.2 wt.% (volatile-free) and low FeO/MgO ratios (Fig. 4f). They exhibit high compatible element concentrations with variable Cr (52.4–282 ppm) and Ni (11–33 ppm) contents. They are characterized by MgO contents (3.13 to 3.88 wt.%) and $Mg^{\#}$ (47–51) [$Mg^{\#} = Mg^{2+} / (Mg^{2+} + Fe^{2+}) \times 100$], that are higher than those of metabasaltic and eclogite experimental melts (Fig. 4c–d) (Rapp et al., 1999), but similar to those of magnesian andesites (e.g., Kelemen et al., 2014; McCarron and Smellie, 1998), such as the Duogecuoren magnesian

Table 1
Major, trace elemental and Sr–Nd isotopic compositions for the Rena Co plutons.

Sample	13GZ02	13GZ03	13GZ04	13GZ05	13GZ08-1	13GZ08-2	13GZ19	13GZ22-1
Type	Granodiorite							
No.	①	①	①	①	①	①	②	②
GPS	84.084°E	84.084°E	84.084°E	84.083°E	84.048°E	84.048°E	84.048°E	84.025°E
	32.889°N	32.889°N	32.889°N	32.889°N	32.889°N	32.889°N	32.889°N	32.768°N
Age (Ma)		151.70						
SiO_2	64.14	64.35	64.55	66.07	63.26	63.62	64.78	66.18
TiO_2	0.70	0.68	0.66	0.60	0.73	0.72	0.63	0.47
Al_2O_3	17.12	16.89	16.81	16.42	17.29	17.09	16.59	16.26
Fe_2O_3 T	4.72	4.63	4.92	3.99	5.03	5.12	4.67	3.27
MnO	0.08	0.08	0.12	0.07	0.08	0.11	0.10	0.08
MgO	1.26	1.21	1.20	1.01	1.31	1.29	1.57	0.91
CaO	4.68	4.75	4.73	4.30	5.05	4.91	3.77	3.16
Na_2O	3.22	3.69	3.22	3.46	3.33	3.23	3.14	3.77
K_2O	2.90	2.71	2.79	3.02	2.75	2.77	3.37	3.26
P_2O_5	0.21	0.21	0.20	0.17	0.22	0.21	0.14	0.10
L.O.I.	0.50	0.32	0.32	0.40	0.46	0.45	0.76	2.07
Total	99.51	99.52	99.51	99.51	99.51	99.52	99.51	99.54
Mg#	35	34	33	33	34	33	40	35
A/CNK	1.01	0.96	0.99	0.98	0.98	0.99	1.06	1.05
T Zr(°C)	823	826	696	821	816	824	776	810
Sc	4.44	4.11	4.27	3.57	4.86	4.80	8.93	3.91
V	25.2	26.6	23.5	22.9	28.2	24.4	48.4	17.5
Cr	190	42.9	43.2	21.4	232	68.8	244	71.1
Co	7.42	6.45	6.93	5.51	7.91	7.19	9.01	4.83
Ni	15.4	3.51	4.56	3.11	18.5	4.27	24.7	4.14
Cu	19.6	3.78	4.44	3.43	23.2	4.20	28.9	3.61
Zn	105	112	115	103	108	113	75.2	91.6
Ga	25.8	26.1	26.5	25.0	25.9	26.2	20.3	24.2
Ge	1.87	2.14	2.19	1.84	2.05	2.13	1.85	1.45
Cs	4.37	4.98	4.55	3.77	3.61	3.66	8.92	2.61
Rb	101	101	97.3	99.5	100	104	126	107
Ba	751	658	696	676	621	647	923	748
Th	10.8	13.2	12.5	9.13	11.9	12.6	7.64	10.3
U	1.40	1.70	1.21	1.43	1.70	1.67	1.26	1.35
Nb	20.7	23.2	22.0	22.7	20.6	20.6	13.4	16.2
Ta	1.48	1.68	1.50	1.68	1.48	1.42	0.96	1.01
La	37.6	47.4	47.1	33.4	40.7	47.4	26.1	34.8
Ce	77.3	97.1	93.9	66.8	84.5	92.1	51.1	63.5
Pb	17.7	18.1	17.2	17.9	17.0	17.8	21.3	20.8
Pr	8.96	11.6	11.2	8.24	9.75	11.1	5.98	7.00
Sr	654	634	640	610	651	635	613	635
Nd	33.4	43.9	41.9	32.0	37.1	41.5	22.3	24.4
Zr	290	323	63	287	286	305	158	227
Hf	7.33	8.44	1.83	7.50	7.27	7.77	4.39	5.94
Sm	6.24	7.83	7.35	6.32	6.79	7.40	4.04	3.78
Eu	1.84	2.03	1.96	1.78	1.92	1.94	1.18	1.07
Gd	4.77	5.60	5.22	4.71	5.05	5.41	3.13	2.71
Tb	0.54	0.60	0.54	0.53	0.57	0.58	0.41	0.28
Dy	2.32	2.35	2.08	2.11	2.43	2.36	2.06	1.17
Y	8.51	7.86	6.80	6.94	8.81	7.98	9.23	4.63
Ho	0.35	0.32	0.27	0.28	0.36	0.33	0.38	0.19
Er	0.73	0.63	0.52	0.52	0.78	0.66	0.94	0.43
Tm	0.09	0.08	0.06	0.06	0.10	0.08	0.14	0.06
Yb	0.55	0.46	0.35	0.34	0.57	0.48	0.82	0.36
Lu	0.08	0.06	0.05	0.05	0.08	0.07	0.13	0.05
$^{87}Sr/^{86}Sr$		0.708150		0.708211		0.708021	0.707960	0.707983
$\pm 2\sigma$		0.000006		0.000007		0.000009	0.000007	0.000008
$(^{87}Sr/^{86}Sr)i$		0.70717		0.70720		0.70701	0.70669	0.70694
$^{143}Nd/^{144}Nd$		0.512346		0.512362		0.512363	0.512340	0.512315
$\pm 2\sigma$		0.000004		0.000004		0.000005	0.000004	0.000005
εNd(t)		−4.0		−3.9		−3.7	−4.2	−4.3
T_{2DM} (Ma)		1274		1267		1247	1287	1302

(*continued on next page*)

Table 1(*continued*)

Sample	13GZ23	13GZ24-1	13GZ24-2	13GZ25	13GZ09-1	13GZ09-2	13GZ10-1	13GZ10-2
Type	Granodiorite				Diorite			
No.	②	②	②	②	③	③	③	③
GPS	84.023°E	84.022°E	84.022°E	84.021°E	84.204°E	84.204°E	84.204°E	84.204°E
	32.768°N	32.768°N	32.768°N	32.769°N	32.79°N	32.79°N	32.784°N	32.784°N
Age (Ma)				148.10	153.00			
SiO_2	63.53	65.74	65.94	64.95	60.14	59.90	60.18	60.43
TiO_2	0.62	0.49	0.49	0.60	0.81	0.82	0.87	0.86
Al_2O_3	17.15	16.41	16.05	16.73	16.54	16.60	16.48	16.50
Fe_2O_3 T	4.43	3.30	3.45	4.39	7.08	7.03	6.90	6.79
MnO	0.08	0.06	0.10	0.09	0.21	0.18	0.16	0.15
MgO	1.60	0.93	0.90	1.60	3.10	3.20	3.12	3.09
CaO	4.24	3.27	2.97	4.00	5.26	5.28	5.13	5.45
Na_2O	3.51	3.91	3.79	3.22	2.74	2.69	2.44	2.48
K_2O	2.91	3.17	3.52	3.03	2.66	2.75	2.78	2.73
P_2O_5	0.13	0.10	0.11	0.13	0.18	0.18	0.20	0.19
L.O.I.	1.33	2.14	2.23	0.91	0.79	0.87	1.25	0.82
Total	99.52	99.52	99.54	99.64	99.52	99.51	99.51	99.50
Mg#	42	36	34	42	46	47	47	47
A/CNK	1.03	1.04	1.04	1.06	0.98	0.98	1.01	0.97
T Zr(°C)	786	816	808	796	762	770	780	776
Sc	7.11	3.83	3.80	6.53	16.7	17.4	17.6	18.5
V	32.0	20.0	18.3	35.8	111	117	106	104
Cr	43.4	247	42.4	38.8	101	72.2	282	198
Co	7.80	6.08	4.44	7.90	14.2	14.3	14.0	13.7
Ni	5.68	19.5	6.03	6.72	15.6	15.2	27.9	24.7
Cu	4.35	23.8	4.61	6.25	6.98	7.65	27.0	23.7
Zn	87.4	92.9	68.7	83.1	87.8	90.3	84.7	86.7
Ga	22.8	24.9	23.2	22.4	20.1	20.5	19.5	19.4
Ge	1.51	1.44	1.50	1.60	2.47	2.47	2.49	2.42
Cs	4.47	2.96	2.13	5.43	7.40	7.45	6.58	6.30
Rb	104	106	121	113	107	110	103	102
Ba	683	737	755	671	615	638	624	568
Th	8.79	10.9	10.7	10.4	7.37	7.70	11.1	7.42
U	1.36	1.47	1.45	1.54	0.65	0.68	1.19	1.08
Nb	12.1	16.8	15.9	11.5	13.8	14.2	12.5	12.5
Ta	0.82	1.05	1.00	0.76	1.05	1.06	0.96	0.98
La	25.9	36.0	35.0	30.8	24.0	24.0	38.0	25.6
Ce	49.2	64.9	64.0	58.8	50.0	48.1	74.1	54.3
Pb	19.8	20.4	19.5	22.4	17.5	18.0	15.9	16.0
Pr	5.74	7.26	7.13	6.68	5.94	6.01	8.93	6.63
Sr	534	656	615	475	460	459	456	422
Nd	21.1	25.1	24.8	23.8	23.2	23.9	33.4	26.3
Zr	189	250	227	201	166	183	194	194
Hf	5.00	6.63	5.93	5.61	4.42	4.79	5.26	5.19
Sm	3.87	3.94	3.89	4.09	4.77	4.90	6.07	5.27
Eu	1.09	1.12	1.07	1.09	1.33	1.34	1.56	1.56
Gd	3.14	2.77	2.77	3.25	4.25	4.35	5.10	4.65
Tb	0.40	0.28	0.28	0.40	0.63	0.65	0.72	0.69
Dy	1.99	1.21	1.19	2.02	3.49	3.64	3.97	3.94
Y	8.27	4.84	4.73	9.39	16.8	17.4	18.8	19.0
Ho	0.35	0.19	0.19	0.35	0.69	0.73	0.78	0.79
Er	0.82	0.45	0.44	0.85	1.84	1.90	2.06	2.12
Tm	0.12	0.06	0.06	0.12	0.28	0.28	0.31	0.32
Yb	0.70	0.38	0.37	0.73	1.74	1.81	1.96	2.02
Lu	0.10	0.06	0.05	0.11	0.27	0.28	0.30	0.31
$^{87}Sr/^{86}Sr$	0.709809			0.710030	0.708556	0.708577		0.708924
$\pm 2\sigma$	0.000007			0.000005	0.000007	0.000008		0.000007
$(^{87}Sr/^{86}Sr)i$	0.70861			0.70856	0.70712	0.70710		0.70743
$^{143}Nd/^{144}Nd$	0.512163			0.512158	0.512285	0.512300		0.512289
$\pm 2\sigma$	0.000004			0.000003	0.000004	0.000005		0.000005
εNd(t)	−7.6			−7.6	−5.5	−5.2		−5.4
T_{2DM} (Ma)	1571			1568	1397	1373		1386

Sample	13GZ11-1	13GZ11-2	13GZ13-1	13GZ13-2	13GZ15-1	13GZ15-2	13GZ20-1	13GZ20-2
Type	Diorite						Granodiorite porphyry	
No.	③	③	④	④	④	④	⑤	⑤
GPS	84.199°E	84.199°E	84.234°E	84.234°E	84.234°E	84.234°E	84.173°E	84.173°E
	32.777°N	32.777°N	32.714°N	32.714°N	32.708°N	32.708°N	32.723°N	32.723°N
Age (Ma)	152.70				148.4 ± 2.5		111.72	
SiO_2	56.91	57.13	59.20	59.41	58.38	58.30	67.09	68.24
TiO_2	0.98	1.01	0.91	0.88	0.87	0.85	0.45	0.44

Table 1 (*continued*)

Sample	13GZ11-1	13GZ11-2	13GZ13-1	13GZ13-2	13GZ15-1	13GZ15-2	13GZ20-1	13GZ20-2
Type	Diorite						Granodiorite porphyry	
No.	③	③	④	④	④	④	⑤	⑤
GPS	84.199°E	84.199°E	84.234°E	84.234°E	84.234°E	84.234°E	84.173°E	84.173°E
	32.777°N	32.777°N	32.714°N	32.714°N	32.708°N	32.708°N	32.723°N	32.723°N
Age (Ma)	152.70				148.4 ± 2.5		111.72	
Al_2O_3	17.16	17.06	16.76	16.61	16.49	16.67	15.31	15.32
Fe_2O_3 T	7.89	7.87	7.38	7.12	7.43	7.64	3.81	3.68
MnO	0.18	0.18	0.15	0.15	0.18	0.18	0.08	0.07
MgO	3.54	3.50	3.39	3.66	3.81	3.77	0.34	0.49
CaO	6.08	6.22	5.49	5.39	5.61	5.54	2.11	1.70
Na_2O	2.74	2.62	2.52	2.50	2.40	2.51	5.47	4.85
K_2O	2.49	2.46	2.63	2.78	2.92	2.90	3.03	2.90
P_2O_5	0.24	0.25	0.21	0.18	0.22	0.20	0.14	0.14
L.O.I.	1.30	1.21	0.87	0.83	1.19	0.95	1.68	1.67
Total	99.52	99.51	99.51	99.50	99.51	99.50	99.51	99.52
Mg#	47	47	48	50	50	49	15	21
A/CNK	0.94	0.93	0.99	0.98	0.95	0.96	0.95	1.08
T Zr(°C)	754	759	768	766	766	762	751	766
Sc	21.1	21.4	19.0	19.4	20.8	21.4	6.81	6.80
V	128	127	125	119	141	144	64.1	51.1
Cr	90.9	52.4	202	67.6	102	117	263	209
Co	14.9	14.5	16.7	17.0	18.3	17.9	7.07	6.90
Ni	13.5	11.2	32.7	20.3	22.6	21.0	41.4	24.1
Cu	5.95	8.22	21.8	7.45	15.8	15.7	39.4	33.0
Zn	103	102	88.2	89.1	91.4	90.1	37.3	39.4
Ga	20.6	20.5	20.6	20.3	20.7	20.4	11.2	12.0
Ge	2.75	2.73	2.51	2.61	2.75	2.64	1.39	1.45
Cs	5.44	4.77	8.74	5.70	5.65	5.68	3.33	4.23
Rb	90.6	89.5	105	107	114	108	76.1	85.3
Ba	564	553	624	655	691	641	980	917
Th	6.54	6.57	8.69	8.13	12.0	9.66	8.65	8.57
U	1.22	1.10	1.08	0.98	1.51	1.13	1.72	1.85
Nb	12.8	13.2	14.3	13.9	16.0	16.3	6.81	6.91
Ta	0.92	0.91	1.03	0.99	1.18	1.17	0.58	0.59
La	29.9	29.7	33.3	29.7	39.7	33.1	21.5	21.8
Ce	62.0	64.2	65.8	57.9	75.2	63.3	39.0	41.0
Pb	13.5	13.2	14.6	15.1	16.3	13.7	15.4	16.0
Pr	8.13	8.13	7.79	7.22	8.94	7.59	4.52	4.57
Sr	497	443	467	474	459	428	438	472
Nd	32.5	32.7	29.9	27.7	33.7	28.8	16.0	16.3
Zr	172	183	178	176	189	177	131	130
Hf	4.57	4.77	4.53	4.54	4.97	4.64	3.40	3.43
Sm	6.47	6.65	5.77	5.44	6.29	5.49	2.74	2.82
Eu	1.67	1.69	1.48	1.48	1.53	1.40	0.73	0.75
Gd	5.64	5.89	5.03	4.81	5.47	4.86	2.33	2.42
Tb	0.83	0.87	0.75	0.70	0.79	0.71	0.33	0.33
Dy	4.67	4.87	4.16	3.99	4.50	4.08	1.85	1.87
Y	21.8	23.7	20.0	19.3	21.6	19.9	8.62	8.61
Ho	0.92	0.97	0.82	0.80	0.91	0.82	0.36	0.38
Er	2.41	2.52	2.17	2.13	2.42	2.22	0.97	1.01
Tm	0.35	0.37	0.32	0.31	0.36	0.33	0.15	0.15
Yb	2.20	2.33	2.02	1.99	2.27	2.10	0.96	1.00
Lu	0.34	0.35	0.31	0.30	0.35	0.32	0.15	0.16
$^{87}Sr/^{86}Sr$	0.708883			0.708761	0.708678		0.707265	0.707359
±2σ	0.000008			0.000008	0.000006		0.000008	0.000008
$(^{87}Sr/^{86}Sr)i$	0.70776			0.70738	0.70714		0.70646	0.70653
$^{143}Nd/^{144}Nd$	0.512296			0.512288	0.512279		0.512577	0.512583
±2σ	0.000004			0.000004	0.000004		0.000004	0.000004
εNd(t)	−5.2			−5.3	−5.4		0.1	0.2
T_{2DM} (Ma)	1374			1383	1389		904	895

Sample	13GZ21-1	13GZ21-2
Type	Granodiorite porphyry	
No.	⑤	⑤
GPS	84.173°E	84.173°E
	32.724°N	32.724°N
Age (Ma)		
SiO_2	65.33	66.04
TiO_2	0.56	0.58
Al_2O_3	14.86	15.13

(*continued on next page*)

Table 1 (*continued*)

Sample	13GZ21-1	13GZ21-2
Type	Granodiorite porphyry	
No.	⑤	⑤
GPS	84.173°E	84.173°E
	32.724°N	32.724°N
Age (Ma)		
Fe_2O_3 T	4.79	4.56
MnO	0.08	0.07
MgO	0.58	0.91
CaO	3.76	3.38
Na_2O	4.20	4.00
K_2O	2.77	2.96
P_2O_5	0.20	0.16
L.O.I.	2.39	1.74
Total	99.53	99.52
Mg#	19	28
A/CNK	0.89	0.95
T Zr(°C)	730	743
Sc	10.1	10.1
V	114	106
Cr	331	310
Co	10.9	9.99
Ni	45.5	41.3
Cu	68.1	61.9
Zn	45.0	45.9
Ga	14.1	14.7
Ge	1.71	1.64
Cs	6.05	6.22
Rb	91.4	104.5
Ba	1029	964
Th	7.73	7.96
U	1.77	2.07
Nb	5.95	6.39
Ta	0.44	0.47
La	24.0	24.1
Ce	44.9	43.8
Pb	11.8	12.4
Pr	5.12	5.02
Sr	484	502
Nd	18.6	18.1
Zr	112	118
Hf	2.94	3.11
Sm	3.14	3.01
Eu	0.81	0.78
Gd	2.57	2.42
Tb	0.33	0.32
Dy	1.82	1.75
Y	8.46	8.23
Ho	0.35	0.35
Er	0.93	0.92
Tm	0.14	0.14
Yb	0.87	0.87
Lu	0.13	0.13
$^{87}Sr/^{86}Sr$	0.706252	
$\pm 2\sigma$	0.000007	
$(^{87}Sr/^{86}Sr)i$	0.70538	
$^{143}Nd/^{144}Nd$	0.512537	
$\pm 2\sigma$	0.000004	
εNd(t)	−0.6	
T_{2DM} (Ma)	966	

Corrected formula as follows (Chu et al., 2006):

$^{87}Sr/^{86}Sr(i) = {}^{87}Sr/^{86}Sr - (^{87}Rb/^{86}Sr)^{*}(e^{\lambda T} - 1)$

$^{87}Rb/^{86}Sr = (Rb/Sr) * 2.8956$

λ (Rb–Sr) = 0.0142 Ga^{-1};

$\varepsilon Nd(T) = [(^{143}Nd/^{144}Nd)_{Sample}(T)/(^{143}Nd/^{144}Nd)_{CHUR}(T) - 1] * 10^4$

λ(Sm–Nd) = 0.00654 Ga^{-1}

$(^{143}Nd/^{144}Nd)_{Sample}(T) = (^{143}Nd/^{144}Nd)_{Sample} - (^{147}Sm/^{144}Nd)_{Sample} * (e^{\lambda T} - 1)$

$^{147}Sm/^{144}Nd = (Sm/Nd) * 0.60456$

$(^{143}Nd/^{144}Nd)_{CHUR}(T) = 0.512638–0.1967 * (e^{\lambda T} - 1)$

$T_{2DM}(Nd) = 1/\lambda * \ln\{1 + [((^{143}Nd/^{144}Nd)_{Sample} - [(^{147}Sm/^{144}Nd)_{Sample} - 0.118] * (e^{\lambda T} - 1) - 0.513151)/(0.118–0.2136)]\}$.

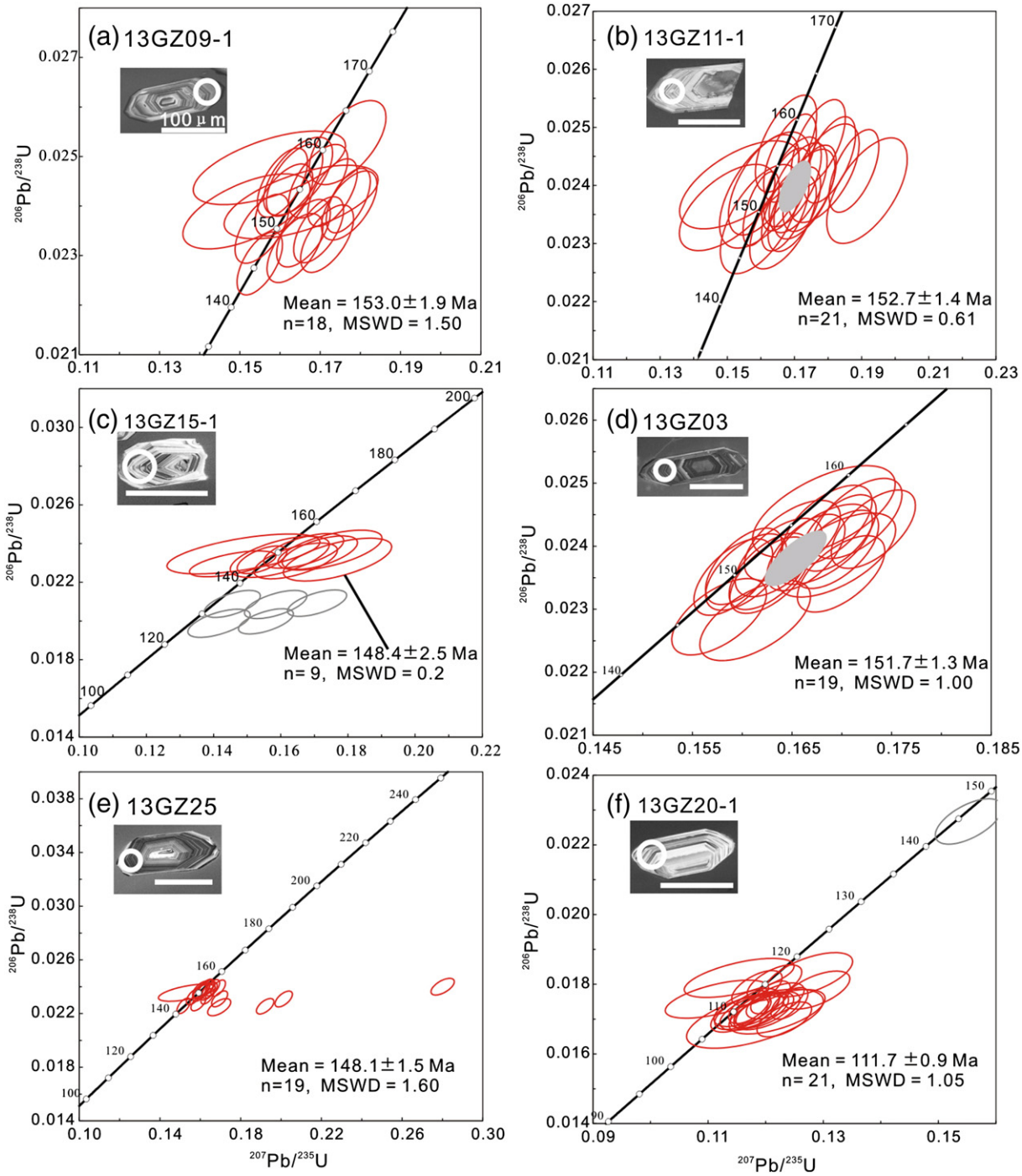

Fig. 3. LA–ICP–MS zircon U–Pb concordia diagrams with CL images for the Rena Co intrusive rocks. (a–c): diorites, (d–e): granodiorites, and (f) granodiorite porphyry.

andesites in central Qiangtang (Wang et al., 2008a). Li et al. (2014b) also reported Late Jurassic dioritic rocks from the Larelaxin and Caima plutons in the southern Qiangtang sub-block with similar magnesian andesite compositions. Therefore, we suggest the Rena Co diorites belong to a regional magnesian diorite suite. It should be noted, however, that these magnesian andesites/diorites are slightly different from typical high-Mg andesites/diorites (e.g., sanukites, Piip-type high-Mg andesites and boninites) in that they have slightly lower MgO contents. The Rena Co magnesian diorites are dominantly metaluminous as indicated by the uniform aluminum saturation index [A/CNK = Al_2O_3/($CaO + Na_2O + K_2O$)] (0.93–0.99) with the exception of one sample (1.01) (Fig. 4e). They show light rare earth element (LREE)-enriched distribution patterns with $(La/Yb)_N$ = 9.1–13.9 and slightly negative Eu anomalies (Eu/Eu^* = 0.79–0.97) (Fig. 6a). On the trace element spider diagram (Fig. 6b), they exhibit a strong enrichment in large ion lithosphere elements (e.g., Cs, Rb, Th, U, K and Pb), a distinct depletion in high field strength elements (e.g., Nb, Ta, Ti, P) and negative Ba anomalies, consistent with typical characteristics of arc-type magmas worldwide.

In the Rena Co area, the granodiorite porphyries (SiO_2 = 67.2–69.7 wt.%) are slightly higher in silica than the granodiorites (SiO_2 = 63.8–67.9 wt.%). Both the granodiorites and granodiorite

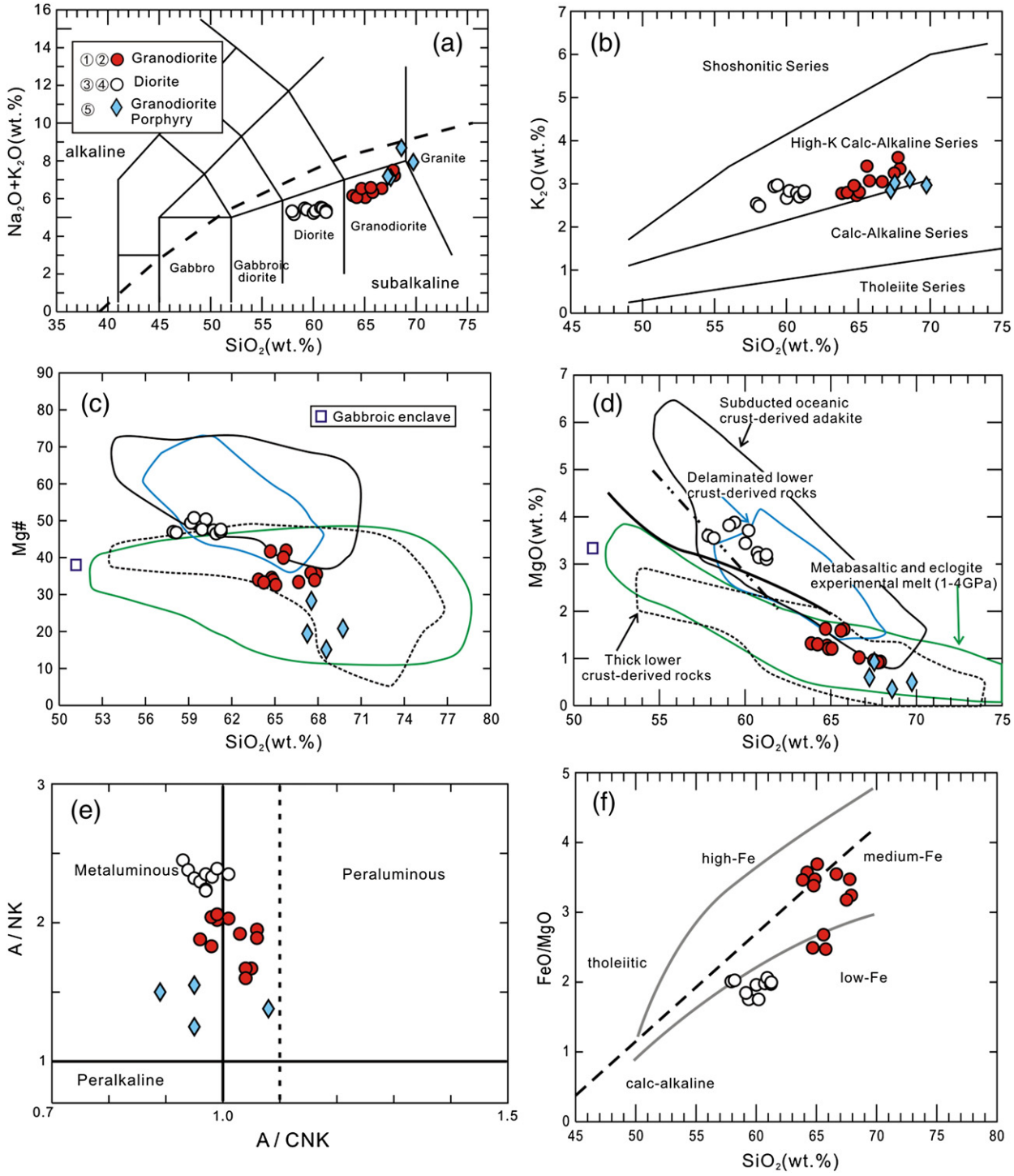

Fig. 4. (a) TAS classification diagram (Middlemost, 1994). (b) K_2O versus SiO_2 diagram. (c): Mg# versus SiO_2. (d): MgO versus SiO_2. Data for metabasaltic and eclogite experimental melts (1–4.0 Ga) are from Rapp et al. (1999) and references therein. The fields of subducted oceanic crust-, delaminated lower crust-, and thickened lower crust-derived adakites are after Wang et al. (2006a,b). Bold solid and dotted lines are two boundaries between magnesian and normal diorites defined by Deng et al. (2009) and McCarron and Smellie (1998), respectively. (e) A/NK versus A/CNK. (f) SiO_2 versus FeO^T/MgO (Miyashiro, 1974).

porphyries are metaluminous to peraluminous with A/CNK values of 0.96–1.08 and 0.89–1.08 (Fig. 4e), sodium-rich with the ratios of Na_2O/K_2O of 0.93–1.36 and 1.35–1.80, respectively (Fig. 5a). They are geochemically characterized by high Al_2O_3 (15.3–17.5 wt.%) (Fig. 5b), low MgO (0.35–1.63 wt.%) and $Mg^{\#}$ (15–42) values (Fig. 4c–d). The granodiorites show subparallel patterns with distinctly enriched light REEs (LREEs) ($[La/Yb]_N$ = 23–96) and negligible Eu anomalies (Eu/Eu^* = 0.92–1.03) on the chondrite-normalized rare earth element diagrams (Fig. 6a), and a strong enrichment in large ion lithosphere elements (e.g., Cs, Rb, Th, U, K, Pb) and a distinct depletion in high field strength elements (e.g., Nb, Ta, Ti, P and heavy REEs) on the extended trace element diagrams (Fig. 6b). The granodiorite porphyries also show LREE enrichments ($[La/Yb]_N$ = 16–20), slightly negative Eu anomalies (Eu/Eu^* = 0.87–0.89) and enrichment of large ion lithophile elements (LILEs) and depletion of HFSEs (Fig. 6). Both the granodiorites and granodiorite porphyries have low Y (4.7–9.4 ppm) and Yb

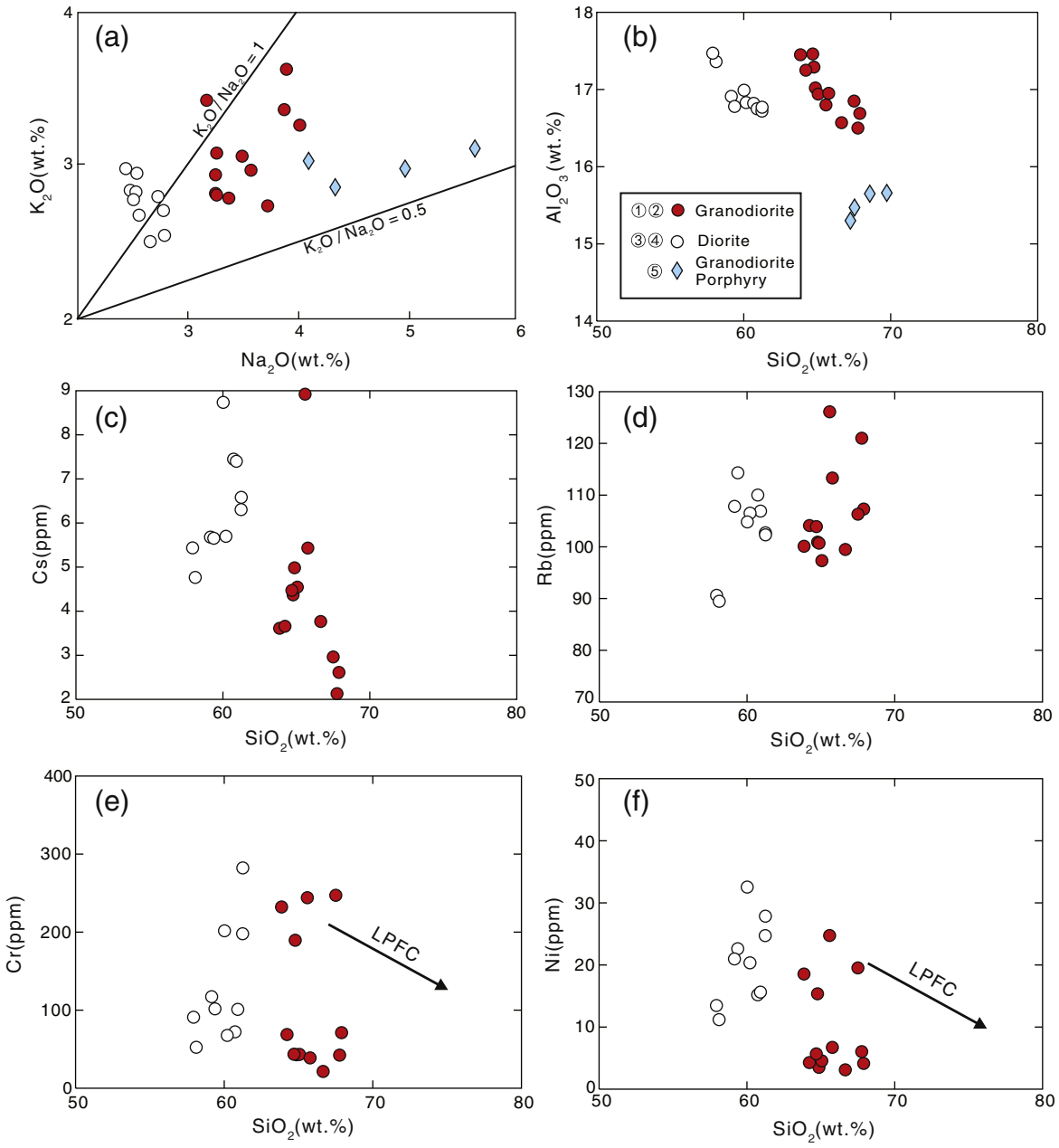

Fig. 5. (a) K_2O versus Na_2O. (b–f) Plots of SiO_2 vs. Al_2O_3, Cs, Rb, Cr, and Ni for the Rena Co intrusive rocks. LPFC, low-pressure fractional crystallization (Castillo et al., 1999).

(0.34–0.99 ppm) contents, high Sr (438–656 ppm) values, resulting in high La/Yb (22–133) and Sr/Y (51–137) ratios. All the above geochemical characteristics indicate they have adakitic affinities (Fig. 7a) as defined by Defant and Drummond (1990).

4.3. Sr–Nd–Hf isotopes

The whole-rock Sr–Nd isotopic data of the Rena Co intrusive rocks are listed in Table 1. The diorites have slightly variable and high initial $^{87}Sr/^{86}Sr$ isotopic ratios (0.7071–0.7078) and constant $\varepsilon_{Nd}(t)$ values of −5.5 to −5.2 corresponding to two-stage Nd model ages (T_{2DM}) of 1373–1397 Ma (Fig. 8). The granodiorite porphyries exhibit low and highly variable $(^{87}Sr/^{86}Sr)_i$ values (0.7054 to 0.7065) but constant $\varepsilon_{Nd}(t)$ values (−0.61 to +0.25) corresponding to T_{2DM} of 895–966 Ma (Fig. 8). The granodiorites, show variable and high $(^{87}Sr/^{86}Sr)_i$ values (0.7069 to 0.7086) and low $\varepsilon_{Nd}(t)$ values (−7.6 to −3.7) (Fig. 8).

Zircon Hf isotopic data are presented in the Supplementary Data. The diorite samples (13GZ09-1, 13GZ11-1 and 13GZ15-1) have a wide range of $\varepsilon_{Hf}(t)$ of −8.6 to +4.9, corresponding to Hf crustal model ages (TC DM) of 895–1748 Ma (Fig. 9). The granodiorites show a wide range of $\varepsilon_{Hf}(t)$ values extending from −9.7 to +0.2 with TC DM values of 1190–1814 Ma (Fig. 9). Except for one inherited zircon (145 Ma) with a low $\varepsilon_{Hf}(t)$ value (+1.0), the granodiorite porphyries have a narrow range of $\varepsilon_{Hf}(t)$ of +4.6 to +9.7 with TC DM values of 550–874 Ma (Fig. 9).

5. Discussion

5.1. Late Mesozoic magmatism in southern Qiangtang

Our new zircon U–Pb age data, together with currently available high-quality zircon U–Pb geochronological data (e.g., Chang et al., 2011; Kapp et al., 2005; Li et al., 2011, 2013, 2014a,b; Liu et al., 2012, 2014; Zhang, 2007; Zhang et al., 2012a), corroborate the presence of a Middle Jurassic–Early Cretaceous continental arc extending ca. 1100 km along the length of southern Qiangtang sub-block from

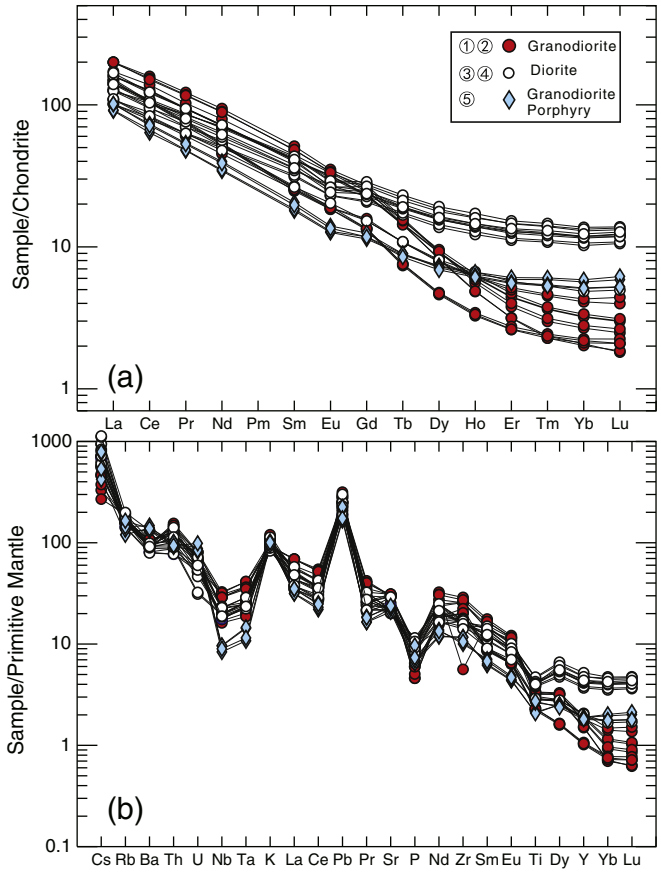

Fig. 6. Chondrite-normalized REE patterns (a) and primitive mantle normalized trace element diagrams (b) for the Rena Co intrusive rocks. Chondrite and primitive mantle normalized values are from Sun and McDonough (1989).

Rotug to Amdo (Fig. 11a). Nevertheless, it should be noted that this 170–102 Ma continental arc is younger than the arc proposed by Guynn et al. (2006) on the basis of the 185–170 Ma granitoids from the Amdo area. In fact, the Amdo block has been interpreted as an isolated microcontinent in the Tethyan Ocean that experienced complex tectono-thermal events, such as Jurassic (~190–170 Ma) high-pressure granulite-facies metamorphism (e.g., Guynn et al., 2013; Zhang et al., 2012b, 2014b). Therefore, the coeval (Early Jurassic) magmatism in the Amdo microcontinent may have been related to deep subduction of this microcontinent beneath southern Qiangtang in a collisional setting rather than to northward subduction of the Bangong–Nujiang Ocean (e.g., Guynn et al., 2013; Zhang et al., 2012b, 2014b).

Late Mesozoic magmatism in the region has been widely attributed to the northward subduction of the Bangong–Nujiang oceanic lithosphere (Geng et al., 2011; Li et al., 2013, 2014a,b; Liu et al., 2014). From ~140 to ~130 Ma, however, there is a noticeable magmatic gap (Fig. 11a). Similar magmatic lulls occur in the Andes and southern Gangdese areas in response to flat or low-angel subduction (e.g., Coulon et al., 1986; Ma et al., 2013a,b; Zhang et al., 2012a). The renewal of magmatism following this gap is considered to be the result of slab roll-back and rapid steepening of the subducting slab (e.g., Ma et al., 2013a,b). During the transition process from flat- to normal angle subduction, upwelling asthenospheric mantle would induce intense magmatism. Therefore, we suggest that the slab roll-back process also accounts for the renewed Early Cretaceous magmatism in southern Qiangtang after the ~140 to ~130 Ma gap. In southern Qiangtang, there appears to be a young age trend from north to south, consistent with the slab roll-back model. It also should be noted that there is a magmatic flare-up at 118 ± 6 Ma in Early Cretaceous (Fig. 11a).

5.2. Petrogenesis

5.2.1. Relationship between granodiorites and diorites

The Rena Co granodiorites and diorites are contemporaneous, however, they are unlikely to have originated from a common parent magma based on the following evidence. First, if the granodiorites evolved from the diorites by fractional crystallization, then the most abundant phase in the diorites, plagioclase, should be a common fractionated phase. However, although the Al_2O_3 contents of both the diorites and granodiorites display decreasing trends with increasing SiO_2 contents, the trends do not overlap to form a common trend, which is inconsistent with a diorite fractionation origin for the granodiorites (Fig. 5b) (e.g., Chen et al., 2010; Li et al., 2014b). Similarly, if diorites and granodiorites were derived from a common source, then the dioritic magma should have higher Cr and Ni plus lower Cs and Rb than granitic magma because the latter would experience more fractionation of mafic minerals and plagioclase (e.g., Chen et al., 2010; Li et al., 2014b). However, in our study, they do not display such trends (Fig. 5c–f), indicating that they were unlikely to have originated from a common parent magma. In addition, some diorite samples are potassium-rich while most granodiorites are sodium-rich, empirically suggesting that they cannot have been derived from the same magma (Fig. 5a). Finally, the diorites exhibit lower $\varepsilon_{Nd}(t)$ and higher initial $^{87}Sr/^{86}Sr$ and $\varepsilon_{Hf}(t)$ than those of most of the granodiorites (Figs. 8, 9), which is inconsistent with AFC (assimilation and fractional crystallization) or magma mixing models. Therefore, the diorites and granodiorites could not have a common source.

5.2.2. Granodiorites

Several models have been proposed for the generation of adakitic rocks such as the Rena Co granodiorites, including (a) melting of subducted young and hot oceanic crust, generally followed by interaction with the overlying mantle wedge (Defant and Drummond, 1990; Rapp et al., 1999); (b) high-pressure fractional crystallization (involving garnet) of basaltic melts (Macpherson et al., 2006); (c) crustal assimilation and low pressure fractional crystallization process from parental basaltic magmas (Castillo et al., 1999); (d) magma mixing between felsic and basaltic magmas (Guo et al., 2007; Streck et al., 2007); (e) melting of delaminated lower continental crust (Gao et al., 2004; Wang et al., 2006b; Xu et al., 2002); (f) melting of the subducted continental crust (Wang et al., 2008a); and (g) melting of thickened mafic lower continental crust (Atherton and Petford, 1993; Chung et al., 2003; Wang et al., 2005). We consider these alternative processes in the following sections with specific reference to the Rena Co adakitic granodiorites.

First, the distinctive geochemical characteristics of the Rena Co adakitic granodiorites indicate that they could not have been generated by partial melting of subducted Bangong–Nujiang oceanic crust. The geochemical compositions of oceanic slab-derived adakites are usually controlled by the basaltic portions of the slabs rather than the overlying sediments. For example, this type of adakite generally has mid-ocean-ridge basalt (MORB)-like Sr–Nd isotopic compositions, and relatively low K_2O, Th and Th/La values (Wang et al., 2008a), even if in some cases, particular slab-derived adakites were formed from the mixing of melts from altered oceanic crust and sediment-derived melts (e.g., Tang et al., 2010). The Rena Co adakitic granodiorites, however, have much more enriched Sr–Nd isotopic compositions, which are very distinct from those of Mesozoic oceanic basalts found in ophiolites along the Bangong–Nujiang Suture (Fig. 8) (e.g., Bao et al., 2007; Zhang et al., 2014a; Zhu et al., 2006b). Their K_2O, Th and Th/La values are also higher than those of MORB and slab-derived adakites (Tang et al., 2010; Wang et al., 2007) (Fig. 7b). Their Sr–Nd isotopic compositions likely represent those of their source because they have $Mg^{\#}$ (32–42) values that are lower than those (>47) of metabasaltic rock-derived experimental melts contaminated by mantle peridotites (Rapp et al., 1999). Accordingly, interaction between felsic magmas and fertilized mantle

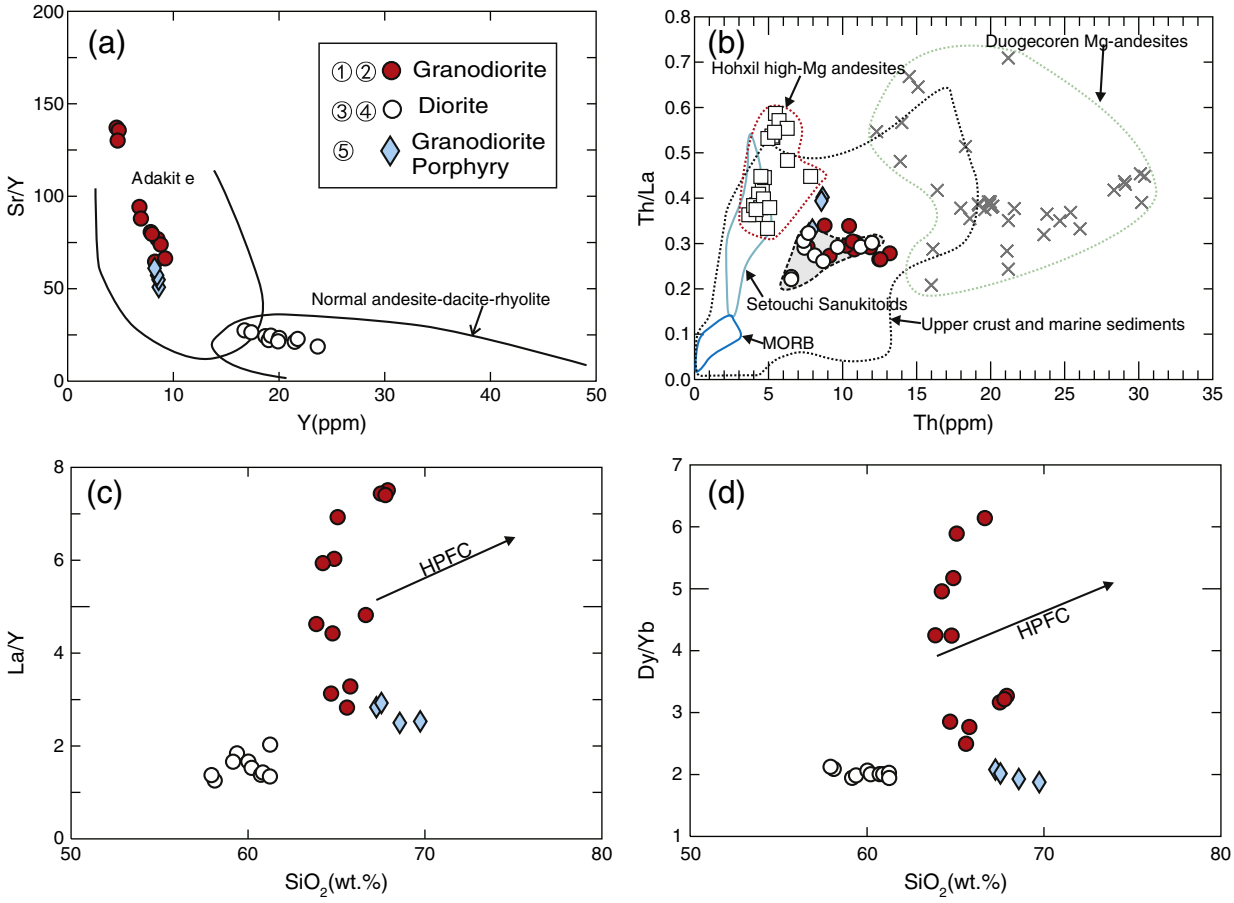

Fig. 7. (a) Y (ppm) versus Sr/Y diagram (Defant and Drummond, 1993). (b) Th versus Th/La diagram. Upper crust and sediments are from Plank and Langmuir (1998) and Plank (2005). The field of MORB is from Niu and Batiza (1997). The Setouchi Sanukitoids in SW Japan are from Shimoda et al. (1998) and Tatsumi (2001). The data for the Hohxil magnesian andesites are from Wang et al. (2011) and for the Duogecuoren Mg-andesites are from Wang et al. (2008a). (c) La/Y versus SiO_2. (d) Dy/Yb versus SiO_2. HPFC, high-pressure fractional crystallization involving garnet (Macpherson et al., 2006).

was unlikely. In addition, some of the granodiorite samples in this study are peraluminous (Fig. 4e) whereas slab-derived adakites are mainly metaluminous (Wang et al., 2008a).

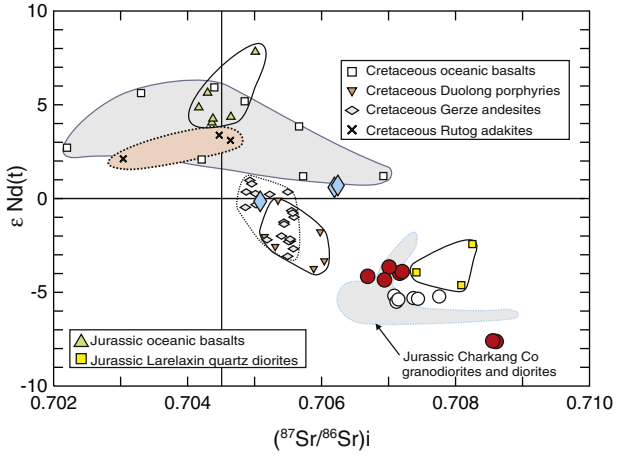

Fig. 8. εNd(t) versus ($^{87}Sr/^{86}Sr$)i. Data for the Jurassic and Cretaceous oceanic basalts are from Bao et al. (2007), Zhang et al. (2014a) and Zhu et al. (2006b). Data for the Cretaceous Rutog adakites and Jurassic Larelaxin granites are from Liu et al. (2014). Data for the Cretaceous Duolong granodiorite porphyries, Gerze andesites and Jurassic Chaerkang granodiorites and diorites are from Li et al. (2013), Liu et al. (2012) and Zhang (2007), respectively. Note that Sr and Nd isotopic data are all corrected to 150 Ma.

Second, it is also unlikely that the Rena Co adakitic granodiorites were generated by high- or low-pressure crystallization from parental basaltic magmas. Suites of adakitic rocks derived from high-pressure fractional crystallization involving a garnet-bearing assemblage will have a wide range of SiO_2 and generally exhibit distinct geochemical trends (Macpherson et al., 2006). In such suites, the La/Y and Dy/Yb ratios clearly increase with the increasing of SiO_2 contents because crystallization of garnet will cause a decrease in HREEs and Y contents. However, the Rena Co adakitic granodiorites display a small range of SiO_2 of 63.8–67.9 wt.% and, rather than showing fractionation trends on La/Y and Dy/Yb versus SiO_2 diagrams (Fig. 7c,d), they define near-vertical trends. During low-pressure fractional crystallization involving olivine and pyroxene, the derived magmas should show a clear decrease in $Mg^{\#}$ values, Cr and Ni contents with the increasing SiO_2 contents (Castillo et al., 1999) but no such trends occur for the Rena Co adakitic granodiorites (Figs. 4c, and 5e–f). The decreases of MgO and Fe_2O_3 contents with increasing SiO_2 suggest that these rocks probably underwent amphibole fractionation (Fig. 4d) (Ma et al., 2013b). However, amphibole fractionation is typically accompanied by plagioclase removal in natural systems and the Rena Co granodiorites do not show the compositional trends consistent with the net effect of combined amphibole and plagioclase fractionation (Ma et al., 2013b; Moyen, 2009). In addition, Moyen (2009) suggested that amphibole + plagioclase fractionation has little or no potential to actually yield adakitic signatures in the first place because the amount of amphibole that can be formed is limited by the Fe and Mg budget to a small mass fraction (in the region of 20%), strongly reducing its potential effect.

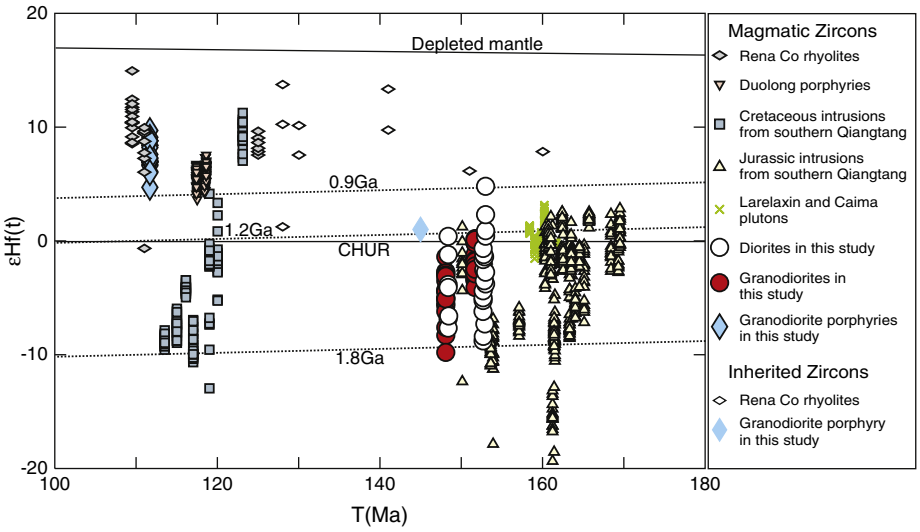

Fig. 9. Plots of εHf(t) (parts per 10^4 deviation of initial Hf isotope rations between zircon samples and the chondritic reservoir at the time of zircon crystallization) versus ages of the Late Mesozoic magmatic rocks in southern Qiangtang sub-block. The sub-horizontal lines are Hf "crustal" model ages (TC DM), which are calculated by assuming its parental magma to have been derived from an average continental crust (with $^{176}Lu/^{177}Hf = 0.015$) that originated from the depleted mantle source (Griffin et al., 2002). Data for the Rena Co rhyolites, the Larelaxin and Caima granitoids are from Chang et al. (2011) and Li et al. (2014b), respectively. The Jurassic and Cretaceous intrusive rocks from southern Qiangtang sub-block are from Li et al. (2014a). Other data are the same as in Fig. 8.

Third, the Rena Co adakitic granodiorites could not be generated by partial melting of the delaminated or subducted continental crust. As a result of contamination by mantle peridotites, adakitic rocks derived from the delaminated lower crust often have higher MgO contents and $Mg^{\#}$ values (Wang et al., 2006b; Xu et al., 2002), than those of the Rena Co adakitic granodiorites. Moreover, lower crust delamination is generally restricted to regions undergoing extension in a continental setting (Wang et al., 2006a,b; Xu et al., 2002). In the Late Jurassic, however, the Rena Co area was in an arc setting related to oceanic subduction (Geng et al., 2011; Li et al., 2014a). In addition, the absence of contemporaneous continental collision largely rules out the possibility that melting of subducted continental crust formed the adakitic granodiorites. In addition, key geochemical characteristics (e.g., Th, Th/La) also do not match those of adakitic rocks derived from subducted continental crust (Fig. 7b) (Wang et al., 2008a).

We therefore suggest that the Rena Co adakitic granodiorites were generated by partial melting of thickened lower continental crust (e.g., Atherton and Petford, 1993; Chung et al., 2003; Wang et al., 2005). Two distinct possible sources (ancient mafic lower crust or newly underplated basaltic juvenile crust) may be delineated using the isotope compositions of adakitic magmas. Ancient mafic lower crust often exhibits more enriched isotopes (e.g., Wang et al., 2005, 2006a) whereas newly underplated basaltic crust, involving mantle-derived materials, often has depleted or less evolved Sr–Nd–Hf isotopic compositions (Wang et al., 2007). In this study, all the granodiorites have enriched Sr–Nd isotopic compositions nearly comparable to those of the existing Larelaxin (Liu et al., 2014) and Charkang Co intrusive rocks (Zhang, 2007) in southern Qiangtang sub-block (Fig. 8) which are considered to be derived from the partial melting of the ancient lower continental crust. In this context, the Rena Co adakites probably indicate crustal thickening. In the plot of La/Yb versus magmatic ages (Fig. 10) (Chung et al., 2009), the La/Yb ratios of the Jurassic intermediate–felsic rocks in southern Qiangtang gradually increased from 10 to 150 corresponding to crustal thickening from 30 km to >50 km between ~170 Ma and ~145 Ma. This gradual thickening was probably due to northward subduction of the Bangong–Nujiang Ocean given that it is a common geological phenomenon in arc settings. The same process occurred in central and northern Lhasa as exemplified by the occurrence of ~112 Ma adakitic rocks (Sui et al., 2013) and ~140 Ma leucogranite produced by anatexis during crustal thickening (Ding and Lai, 2003). Numerous Late Cretaceous (~90 Ma) magnesian andesites/diorites also indicate the subsequent delamination of the thickened lithospheric following the final Lhasa–Qiangtang amalgamation (e.g., Wang et al., 2014). Taking into account the closure of the Bangong–Nujiang Ocean at ~ 100 Ma, it is likely that the lithosphere had probably already been thickened during prior subduction, allowing for the generation of the Rena Co adakitic granodiorites.

It should be noted that the variable Sr–Nd isotopes of these granodiorites can be attributed to either a heterogeneous lower continental crust source or magma mixing between crust-derived melts and mantle-derived melts. In the latter case, strong correlations are expected between isotopes and chemical components but none are evident between Sr, Nd isotopic compositions and SiO_2, MgO or Sm/Nd. Given the lack of mafic microgranular enclaves (MMEs) observed in the field, we suggest the granodiorites were probably derived from a thick and heterogeneous lower continental crust source. This scenario is also supported by the overall negative εHf(t) values of zircons in the granodiorites (Fig. 9), which demonstrate that the Rena Co adakitic granodiorites could be generated from such a source.

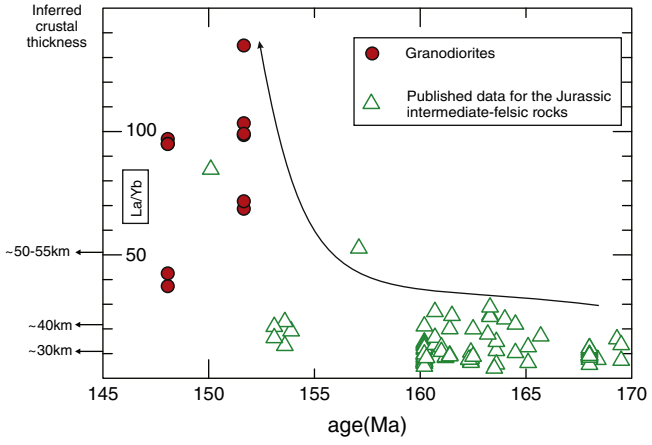

Fig. 10. Plot of La/Yb ratios versus magmatic ages for the Jurassic intermediate-felsic rocks in southern Qiangtang (from the diagram of Chung et al. (2009)), with published data from Li et al. (2014a,b), Liu et al. (2014).

5.2.3. Diorites

In a continental arc, intermediate magmatic rocks are generally considered to form by the crystallization of mantle-derived basaltic magmas or the interaction between hot basaltic magmas and felsic magmas in MASH zones (melting, assimilation, storage, and homogenization) (Annen et al., 2006). In the case of high-Mg andesites (HMA) and their Mg-rich diorite derivatives (Kamei et al., 2004; Shimoda et al., 1998), however, a variety of models may account for their petrogenesis, including hydrous melting of peridotites (Falloon and Danyushesky, 2000; Tatsumi, 2001; Taylor et al., 1994), mixing between mantle-derived basaltic magma and crust-derived felsic melt (Guo et al., 2007; Streck et al., 2007), or the interaction between slab-derived melts and mantle wedge peridotites (e.g., Shimoda et al., 1998; Tang et al., 2010; Tatsumi, 2001; Tatsumi and Hanyu, 2003; Wang et al., 2008b, 2011).

We argue that the first two models are not applicable to the Rena Co magnesian/Mg-rich diorites based on the following observations. First, although the coeval gabbroic enclaves reported by Li et al. (2014b) cannot be considered to represent primary basaltic magma, they still should have higher MgO contents than diorites because diorites probably experienced more extensive fractional crystallization of mafic minerals and plagioclase if diorites and gabbroic enclaves were derived from a common mantle source. Therefore, the relatively lower MgO contents of coeval gabbroic enclaves than the diorites could preclude magma mixing and AFC for the formation of the Rena Co magnesian diorites. In addition, magnesian andesites/diorites formed by magma mixing between mantle-derived basaltic and crust-derived felsic magmas usually have adakitic affinities (Guo et al., 2007; Streck et al., 2007), but the Rena Co diorites do not plot in the adakites field (Fig. 7a). Moreover, the Rena Co diorites differ from boninites in the Bonin Island (Japan), which are high-Mg magmas derived directly from partial melting of the mantle wedge peridotites fluxed by slab-derived H_2O-rich fluids (Falloon and Danyushesky, 2000). The diorites have higher TiO_2 (0.82–1.02 wt.%) and Al_2O_3 (16.72–17.47 wt.%) contents than boninites that typically have TiO_2 < 0.5 wt.% and Al_2O_3 < 15 wt.% (Taylor et al., 1994). In addition, the Rena Co diorites have high Th (6.5–12 ppm) and Nb (12.5–16 ppm) contents and Th/La (0.22–0.32) ratios, indicating the metasomatic agents are slab-melts rather than slab-fluids because HFSEs are insoluble in fluids but compatible in melts (e.g., Class et al., 2000).

Alternatively, the interaction between subducted-slab-derived melts and overlying mantle peridotites has been increasingly considered as a possible mechanism for generation of magnesian magmas (Kelemen et al., 2014; Shimoda et al., 1998; Tang et al., 2010; Tatsumi, 2001; Tatsumi and Hanyu, 2003; Wang et al., 2007, 2008b, 2011). Such melts can be derived from either subducted sediments alone or oceanic crust with variable proportions of overlying sediments. We suggest the Rena Co magnesian diorites probably originated from sediment-derived melts for the following two reasons. On the one hand, they exhibit relatively high initial $^{87}Sr/^{86}Sr$ and low $\varepsilon_{Nd}(t)$, which are very distinct from those of Jurassic basalts (Fig. 8) or mixtures of basalt-derived melts and oceanic sediment-derived melts (Tang et al., 2010; Tatsumi, 2001; Tatsumi and Hanyu, 2003). On the other hand, their Th contents (6.6–12 ppm) and Th/La ratios (0.22–0.32) are similar to those of marine sediments or upper crust and they resemble those of the Hohxil magnesian andesites, which are distinctly higher than those of MORB (Wang et al., 2011). The Hohxil magnesian andesites were generated by the interaction between subducting sediment-derived melts and mantle wedge peridotites (Wang et al., 2011). Tatsumi (2001) suggested that the composition of a sediment-derived melt could change from rhyolitic to andesitic (or dioritic) as it dissolved olivine and clinopyroxene in mantle peridotites. Qian and Hermann (2010) also proposed that the interaction of felsic melts with ultramafic material can produce Mg-rich rocks.

Based on a recent experimental study, however, Mann and Schmidt (2015) concluded that fluid-saturated melting of subducting sediments at sub-arc depths is not sufficient to effectively transfer trace elements such as LILE because of the stability of phengite. Fluid-absent melting, however, requires high temperatures of >850 °C at sub-arc depths, which are not reached in most subduction zones. Behn et al. (2011) also suggested that the trace elements that form sediment melt signature are retained in the sediments until the rocks have experienced temperatures exceeding 1050 °C. Thus, according to subduction zone thermal models, these temperatures are much higher than those at the surface of subducted slabs at the relevant pressures. Nonetheless, a sediment imprint including high Th contents and Th/La ratios exists in many arc rocks, including the Rena Co diorites. An alternative mechanism involves cold sediment diapirs that rise into the mantle wedge and act as the source of the sediment signature in arc rocks (e.g., Behn et al., 2011; Mann and Schmidt, 2015). In this model, subducted sediments detach from the downgoing slab at temperatures of 500–850 °C to form buoyant diapirs. The diapirs rise through the overlying hot mantle wedge, where temperatures exceed 1050 °C, undergo dehydration melting, and release the trace elements that later form the sediment melt signature in arc rocks (e.g., Behn et al., 2011; Marschall and Schumacher, 2012). A wide range zircon $\varepsilon Hf(t)$ values from −8.7 to +4.8 (up to 13-ε units) in the Rena Co magnesian diorites is consistent with the interaction of sediment diapirs-derived melts and asthenosphere mantle-derived melts and we therefore suggest that oceanic sediment diapirs are a likely source for the Rena Co magnesian diorites.

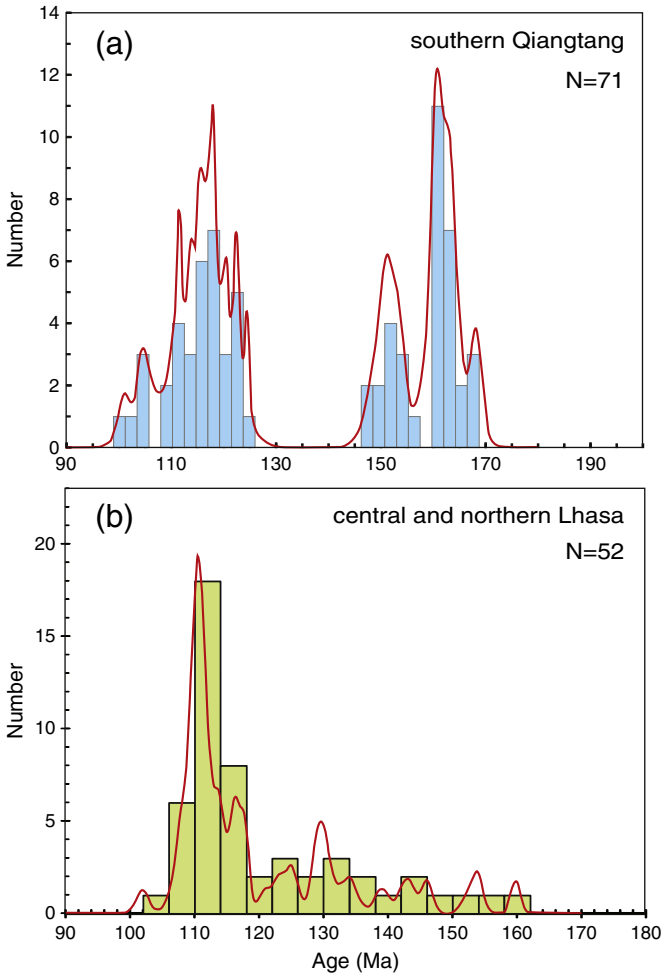

Fig. 11. Histograms of age dates for Late Mesozoic magmatic rocks in southern Qiangtang sub-block (a) and central and northern Lhasa sub-block (b).
Data sources: (Chang et al., 2011; Kapp et al., 2005; Li et al., 2011, 2013, 2014a,b; Liu et al., 2012, 2014; Sui et al., 2013; Zhang, 2007; Zhu et al., 2009, 2011; this study).

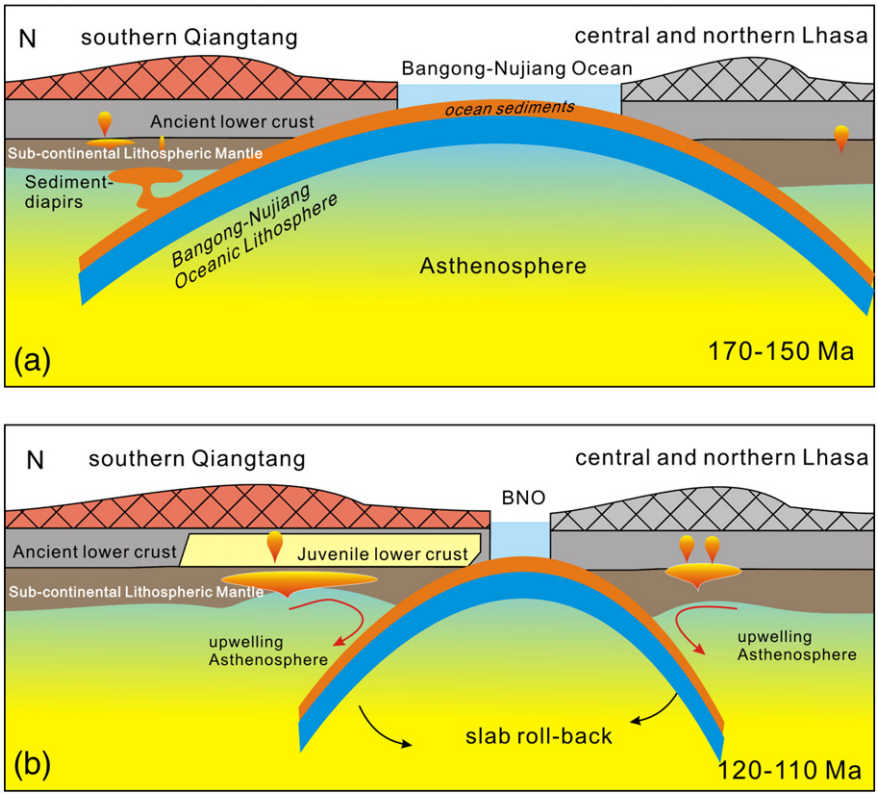

Fig. 12. A conceptual model illustrating the tectonic and magmatic rock evolution of central Tibet during the Late Mesozoic. (a) In the Late Jurassic, sediment diapirs melted and ascended through mantle wedge to form the Rena Co magnesian diorites. Meanwhile, mantle-derived magmas underplated and provided heat to prompt partial melting of the thickened and heterogeneous ancient crust to generate the Rena Co adakitic granodiorites. (b) In the Early Cretaceous, partial melting of the newly underplated basaltic crust at 118 ± 6 Ma resulted in formation of the Rena Co granodiorite porphyries. Magmatic flare-ups occurred in both southern Qiangtang and central and northern Lhasa sub-blocks as a result of slab roll-back.

5.2.4. Granodiorite porphyries

The Early Cretaceous Rena Co adakitic granodiorite porphyries have much in common with the Late Jurassic adakitic granodiorites discussed above, which might suggest a similar petrogenesis. Their Sr–Nd isotopic compositions, however, are distinct from those of the ancient lower crust-derived Jurassic adakitic granodiorites in the Rena Co area, the Cretaceous and Jurassic oceanic basalts in the Bangong–Nujiang Suture Zone (Bao et al., 2007; Zhang et al., 2014a; Zhu et al., 2006b), or adakitic granites in the Rutog area that were derived from subducted Bangong–Nujiang Oceanic crust (Liu et al., 2014) (Fig. 8). Instead, their Sr–Nd isotopic compositions are similar to those of the Early Cretaceous andesites in the Gerze area (ca. 124 Ma) and granodiorite porphyries in the Duolong area (ca. 118 Ma), which recent studies link to fractionated products of basaltic melts derived from mantle wedge peridotites (Li et al., 2013; Liu et al., 2012). In addition, their εHf(t) values of +4.7 to +9.7 are similar to those of the Early Cretaceous granodiorite porphyries (ca. 118 Ma) in the Duolong area (Li et al., 2013) and rhyolites in the Rena Co area (ca. 110 Ma) (Chang et al., 2011) (Fig. 9) and consistent with derivation from juvenile crust. An inherited zircon from sample 13GZ20-1 exhibits an slightly older age of 145 Ma and positive $\varepsilon_{Hf}(t)$ of +1.0, which is also feature of the Rena Co rhyolites (ca. 110 Ma) where numerous inherited zircons show slightly older ages of 160–125 Ma and positive $\varepsilon_{Hf}(t)$ values (Chang et al., 2011) (Fig. 9). This suggests that the basaltic source rocks of these Early Cretaceous rocks, which may have been underplated at the base of southern Qiangtang sub-block since Late Jurassic, melt and produce the Early Cretaceous felsic magmas. Hence, the characteristic of the Early Cretaceous rocks would inherited from the juvenile basaltic source rocks. For example, the Rena Co adakitic granodiorite porphyries show positive zircon $\varepsilon_{Hf}(t)$ values of +4.7 to +9.7 and corresponding whole-rock $\varepsilon_{Nd}(t)$ ranging from −0.61 to +0.25, indicating a decoupling of Hf and Nd isotopic compositions from the mantle (Chauvel et al., 2008) and crustal arrays (Vervoort et al., 1999). The same feature was also reported in the Duolong granodiorite porphyries by Li et al. (2013) who suggested that the decoupling probably inherited from newly underplated basalts. This process can occur in a mantle wedge metasomatized by slab-derived fluid and melt where Nd has a high solubility compared to Hf (Kessel et al., 2005).

Based on the evidence summarized above, we propose a two-stage model for the generation of the Early Cretaceous adakitic granodiorite porphyries in the Rena Co area similar to that presented for the generation of the Cordillera Blanca batholith (Atherton and Petford, 1993). This model emphasizes the input of mafic magmas originating from a metasomatized mantle, forming underplated basaltic lower crust. This thickened juvenile crust later partially melted, producing the adakitic magmas at ca. 112 Ma. It should be noted that there is a significant change in whole-rock Sr–Nd isotopic compositions (Fig. 8) and zircon $\varepsilon_{Hf}(t)$ (Fig. 9) from the Late Jurassic to the Early Cretaceous magmatic rocks. This points to an increased contribution of a mantle or juvenile crust component in the Early Cretaceous igneous rocks in southern Qiangtang sub-block. A similar pattern was documented in central and northern Lhasa by Zhu et al. (2009).

6. Geodynamic processes and implications for crustal growth

6.1. Geodynamic processes

The Bangong–Nujiang Ocean must have survive until the Late Cretaceous because studies of ophiolitic mélanges on the Bangong–Nujiang Suture identify numerous Early Cretaceous oceanic basalts (Bao et al., 2007; Baxter et al., 2009; Xu et al., 2014; Zhang et al., 2014a; Zhu et al., 2006b) where an angular unconformity separates the continental

deposits of the Late Cretaceous Jingzhushan formation from the underlying ophiolitic mélanges (Geng et al., 2011; Xu et al., 2014). However, the subduction polarities of the Bangong–Nujiang Ocean remain the subject of debate. Although some authors have suggested that the Bangong–Nujiang Ocean subducted southward beneath the central and northern Lhasa (Pan et al., 2006; Sui et al., 2013; Zhu et al., 2006a, 2009, 2011, 2013), a larger number of studies have argued that the subduction direction was northward (Ding et al., 2003; Geng et al., 2011; Kapp et al., 2003; Qiu et al., 2005; Qu et al., 2009; Shi et al., 2004; Zhang et al., 2012a) and that the Bangong–Nujiang Ocean began to subduct beneath the southern Qiangtang sub-block in the Late Triassic–Early Jurassic (Qiu et al., 2005; Qu et al., 2009; Shi et al., 2004; Zhang et al., 2012a).

As discussed above, the presence of extensive (>1000 km long) Late Mesozoic continental arc magmatism (170–102 Ma) along the southern Qiangtang sub-block strongly indicates the northward subduction of the Bangong–Nujiang ocean (Fig. 11a) (e.g., Kapp et al., 2005; Li et al., 2014a,b; Liu et al., 2012, 2014). The present study provides additional evidence for this northward subduction because the Rena Co magnesian diorites formed by the interaction of oceanic sediments diapirs-derived melts and mantle wedge peridotites.

In contrast to the evidence provided by the Rena Co rocks, an east–west belt of Late Mesozoic magmatic rocks (164–102 Ma) in central and northern Lhasa (Fig. 11b) have been attributed to the southward subduction of the Bangong–Nujiang Ocean (e.g., Pan et al., 2006; Zhu et al., 2006a, 2009, 2011). A slab break-off model has also been suggested to explain a magmatic flare-up with an increased mantle contribution at 110 ± 3 Ma (Fig. 11b) in the central and northern Lhasa sub-block following the Lhasa–Qiangtang amalgamation at ca. 145 Ma (Sui et al., 2013; Zhu et al., 2009, 2011). However, we note that an identical magmatic flare-up, also accompanied by an increased contribution of a mantle component, occurred in the southern Qiangtang sub-block at 118 ± 6 Ma (Figs. 9 and 10a). If the Bangong–Nujiang oceanic basin remained open in the Early Cretaceous, as suggested above, then it is difficult for a slab break-off model to account for contemporary magmatic flare-ups in both southern Qiangtang and central and northern Lhasa sub-blocks during the Late Early Cretaceous.

The bidirectional subduction of the Bangong–Nujiang Ocean has recently been suggested (Xu et al., 2014; Zhang, 2007; Zhu et al., 2016), and such a scenario can better account for the twin magmatic flare ups if slab break-off events did not occur. We suggest that, during Late Mesozoic, the Bangong–Nujiang oceanic basin most probably subducted both northward under southern Qiangtang and southward under central and northern Lhasa, respectively (Fig. 12). This model can account for the formation of the Rena Co intrusive rocks, including the Late Jurassic adakitic granodiorites and magnesian diorites and the Early Cretaceous adakitic granodiorite porphyries in the southern Qiangtang sub-block, while still allowing for later final closure of the Bangong–Nujiang oceanic basin (Fig. 12).

In this model, sediments detach from the downgoing slab during northward subduction (from ~170 Ma to ~140 Ma) and form buoyant diapirs (Fig. 12a). The diapirs rise, melt and interact with the surrounding mantle wedge to generate the Rena Co magnesian diorites. Contemporaneous basaltic magmas derived from the mantle wedge underplate the base of the southern Qiangtang sub-block crust, providing heat and material for partial melting of the older lower crust, resulting in the generation of intermediate-felsic magmas (Chang et al., 2011; Kapp et al., 2005; Li et al., 2011, 2013, 2014a,b; Liu et al., 2012, 2014) and the Rena Co adakitic granodiorites, given that local crustal thickness was >45 km. The basaltic underplating would gradually replace the ancient lower crust and accumulate to form juvenile crust. This newly underplated basaltic crust would be heated further by the upwelling asthenosphere as a result of Early Cretaceous slab roll-back, resulting in, melting and the generation of the Rena Co adakitic granodiorite porphyries at ca. 112 Ma (Fig. 12b). This mechanism may also apply to the geological processes in central and northern Lhasa (Fig. 12b).

6.2. Implications for crustal growth

The Tibetan plateau is characterized by the thickest continental crust (60–80 km) on Earth, twice as thick as average continental crust (Kind et al., 1996; Mo et al., 2007). Crustal thickening is often largely attributed to tectonic effects (e.g., Ding et al., 2003; Harrison et al., 1992; Kapp et al., 2005; Yin and Harrison, 2000) but magmatic contributions are also important for the formation of thickened juvenile crust (e.g., Chu et al., 2006; Chung et al., 2003; Ji et al., 2009; Ma et al., 2013a, 2013b; Mo et al., 2007, 2008; Niu, 2009; Wang et al., 2005; Zhang et al., 2014c; Zhu et al., 2009, 2011).

Previous Nd–Hf isotopic studies highlighted the importance of mantle and oceanic crust contributions to the crustal growth of southern Tibet in association with the Neo-Tethyan Ocean northward subduction and the India–Asia continental collision since the Mesozoic (Chu et al., 2006; Chung et al., 2003; Ji et al., 2009; Ma et al., 2013a; Mo et al., 2007; Zhang et al., 2014c). The geodynamics of Late Mesozoic crustal growth in central Tibet, however, have not been clear. For example, recent geochemical investigations have revealed that basalt underplating-related vertical crustal growth may have occurred in the continent–continent collision setting of the central and northern Lhasa sub-block, central Tibet (Sui et al., 2013; Zhu et al., 2009, 2011). Conversely, Zhang et al. (2014a) reported the occurrence of a Meso-Tethyan oceanic plateau in the Bangong–Nujiang Ocean in Late Mesozoic (193–173 Ma and 128–104 Ma), implying that oceanic plateau accretion contributed to lateral crustal growth in the southern Qiangtang sub-block.

In the present study, taking into account ophiolites in the Bangong–Nujiang Suture (Bao et al., 2007; Zhang et al., 2014a; Zhu et al., 2006b) and the nature of Late Mesozoic magmatic rocks (e.g., Kapp et al., 2005; Li et al., 2014a,b; Liu et al., 2012, 2014; Sui et al., 2013; Zhu et al., 2009, 2011, 2016; this study) in southern Qiangtang and central and northern Lhasa sub-blocks, we suggest that both southern Qiangtang and central and northern Lhasa sub-blocks were located in continental arc settings related to bidirectional subduction of the Bangong–Nujiang oceanic basin as outlined above (Zhu et al., 2016; this study).

The data obtained in this study and in the literature (e.g., Chang et al., 2011; Li et al., 2013, 2014a,b; Liu et al., 2012, 2014), together with the foregoing discussion, indicate an important role for underplated basaltic magmas in the vertical crustal growth in a continental arc, as exemplified by the Reno Co Early Cretaceous granodiorite porphyries.

In terms of Nd–Hf isotopic compositions (Figs. 8, 9), the Jurassic intermediate–felsic intrusive rocks of the southern Qiangtang sub-block primarily exhibit negative whole-rock εNd(t) and zircon εHf(t) (Li et al., 2014a,b; Liu et al., 2014; this study), indicating that they were largely derived from mature or recycled continental crust materials. In contrast, the Early Cretaceous magmatic rocks from the southern Qiangtang sub-block mainly show positive to near-zero εNd(t) and positive εHf(t) values (Chang et al., 2011; Li et al., 2013, 2014a; Liu et al., 2012, 2014; this study), indicating they were probably derived from the juvenile crust. These results imply that the ancient lower crust of southern Qiangtang sub-block was gradually replaced by mantle-derived juvenile materials between the Late Jurassic and Early Cretaceous and that the underplating of arc basaltic magmas played a key role in vertical crustal growth.

7. Conclusions

(1) The Rena Co intrusive rocks from southern Qiangtang sub-block contain adakitic granodiorites and granodiorite porphyries, and magnesian diorites.
(2) LA–ICP–MS zircon U–Pb dating suggests that the Rena Co granodiorites and diorites have consistent ages of ca. 150 Ma and were emplaced in Late Jurassic and that the granodiorite porphyries were emplaced at ca. 112 Ma in Early Cretaceous.

(3) The Jurassic magmatism was related to northward subduction of the Bangong–Nujiang Oceanic basin and the Early Cretaceous magmatism was most plausibly the result of the slab roll-back. The granodiorites were probably produced by partial melting of a thickened and heterogeneous ancient mafic lower continental crust whereas the diorites were derived from sediment diapirs and the mantle wedge. The younger granodiorite porphyries were generated by partial melting of newly underplated basaltic crust.

(4) In southern Qiangtang, the pre-existing lower crust was gradually replaced by mantle-derived juvenile materials between the Late Jurassic and Early Cretaceous. This process demonstrates that, in a continental arc, underplating of arc basaltic magmas plays a key role in vertical crustal growth.

Supplementary data to this article can be found online at http://dx.doi.org/10.1016/j.lithos.2015.09.015.

Acknowledgments

We would like to thank Editor-in-Chief Professor Sun-Lin Chung, Guest Editor Dr. Di-Cheng Zhu and two anonymous reviewers for their constructive and helpful reviews. We also appreciate the assistance of Yue-Heng Yang, Xi-Rong Liang, Xiang-Lin Tu, Jin-Long Ma, Guang-Qian Hu, Lie-Wen Xie and Ying Liu for zircon age and geochemical analyses. Financial support for this research was provided by the Strategic Priority Research Program (B) of the Chinese Academy of Sciences (grant no. XDB03010600), the National Natural Science Foundation of China (Nos. 41025006, 41202040 and 41421062) and the Guangzhou Institute of Geochemistry, Chinese Academy of Sciences (GIGCAS 135 project Y234021001). This is contribution no. IS-2143 from GIGCAS.

References

Andersen, T., 2002. Correction of common lead in U–Pb analyses that do not report 204 Pb. Chemical Geology 192, 59–79.
Annen, C., Blundy, J.D., Sparks, R.S.J., 2006. The genesis of intermediate and silicic magmas in deep crustal hot zones. Journal of Petrology 47, 505–539.
Atherton, M.P., Petford, N., 1993. Generation of sodium-rich magmas from newly underplated basaltic crust. Nature 362, 144–146.
Bao, P.S., Xiao, X.C., Su, L., Wang, J., 2007. Petrological, geochemical and chronological constraints for the tectonic setting of the Dongco ophiolite in Tibet. Science in China Series D: Earth Sciences 50, 660–671 (in Chinese with English abstract).
Baxter, A.T., Aitchison, J.C., Zyabrev, S.V., 2009. Radiolarian age constraints on Mesotethyan ocean evolution, and their implications for development of the Bangong–Nujiang suture, Tibet. Journal of the Geological Society 166, 689–694.
Behn, M.D., Kelemen, P.B., Hirth, G., Hacker, B.R., Massonne, H.J., 2011. Diapirs as the source of the sediment signature in arc lavas. Nature Geoscience 4, 641–646.
Belousova, E., Griffin, W.L., O'reilly, S.Y., Fisher, N., 2002. Igneous zircon: trace element composition as an indicator of source rock type. Contributions to Mineralogy and Petrology 143, 602–622.
Castillo, P.R., Janney, P.E., Solidum, R.U., 1999. Petrology and geochemistry of Camiguin Island, southern Philippines: insights to the source of adakites and other lavas in a complex arc setting. Contributions to Mineralogy and Petrology 134, 33–51.
Chang, Q.S., Zhu, D.C., Zhao, Z.D., Dong, G.C., Mo, X.X., Liu, Y.S., Hu, Z.C., 2011. Zircon U–Pb geochronology and Hf isotopes of the Early Cretaceous Rena Co rhyolites from southern margin of Qiangtang, Tibet, and their implications. Acta Petrologica Sinica 27, 2034–2044 (in Chinese with English abstract).
Chauvel, C., Lewin, E., Carpentier, M., Arndt, N.T., Marini, J.C., 2008. Role of recycled oceanic basalt and sediment in generating the Hf–Nd mantle array. Nature Geoscience 1, 64–67.
Chen, B., Arakawa, Y., 2005. Elemental and Nd–Sr isotopic geochemistry of granitoids from the West Junggar foldbelt (NW China), with implications for Phanerozoic continental growth. Geochimica et Cosmochimica Acta 69, 1307–1320.
Chen, J.L., Xu, J.F., Kang, Z.Q., Li, J., 2010. Origin of Cenozoic alkaline potassic volcanic rocks at KonglongXiang, Lhasa terrane, Tibetan Plateau: Products of partial melting of a mafic lower-crustal source? Chemical Geology 273, 286–299.
Chu, M.F., Chung, S.L., Song, B., Liu, D.Y., O'Reilly, S.Y., Pearson, N.J., Ji, J.Q., Wen, D.J., 2006. Zircon U–Pb and Hf isotope constraints on the Mesozoic tectonics and crustal evolution of southern Tibet. Geology 34, 745–748.
Chung, S.L., Liu, D.Y., Ji, J.Q., Chu, M.F., Lee, H.Y., Wen, D.J., Lo, C.H., Lee, T.Y., Qian, Q., Zhang, Q., 2003. Adakites from continental collision zones: melting of thickened lower crust beneath southern Tibet. Geology 31, 1021–1024.
Chung, S.L., Chu, M.F., Zhang, Y.Q., Xie, Y.W., Lo, C.H., Lee, T.Y., Lan, C.Y., Li, X.H., Zhang, Q., Wang, Y.Z., 2005. Tibetan tectonic evolution inferred from spatial and temporal variations in post-collisional magmatism. Earth-Science Reviews 68, 173–196.
Chung, S.L., Chu, M.F., Ji, J.Q., O'Reilly, S.Y., Pearson, N.J., Liu, D.Y., Lee, T.Y., Lo, C.-H., 2009. The nature and timing of crustal thickening in Southern Tibet: geochemical and zircon Hf isotopic constraints from postcollisional adakites. Tectonophysics 477, 36–48.
Class, C., Miller, D.M., Goldstein, S.L., Langmuir, C.H., 2000. Distinguishing melt and fluid subduction components in Umnak Volcanics, Aleutian Arc. Geochemistry, Geophysics, Geosystems 1.
Collins, W.J., 1998. Evaluation of petrogenetic models for Lachlan Fold Belt granitoids: implications for crustal architecture and tectonic models. Australian Journal of Earth Sciences 45, 483–500.
Condie, K.C., 1998. Episodic continental growth and supercontinents: a mantle avalanche connection? Earth and Planetary Science Letters 163, 97–108.
Coulon, C., Maluski, H., Bollinger, C., Wang, S., 1986. Mesozoic and Cenozoic volcanic rocks from central and southern Tibet: 39 Ar–40 Ar dating, petrological characteristics and geodynamical significance. Earth and Planetary Science Letters 79, 281–302.
Defant, M.J., Drummond, M.S., 1990. Derivation of some modern arc magmas by melting of young subducted lithosphere. Nature 347, 662–665.
Defant, M.J., Drummond, M.S., 1993. Mount St. Helens: potential example of the partial melting of the subducted lithosphere in a volcanic arc. Geology 21, 547–550.
Deng, J.F., Flower, M.F., Liu, C., Mo, X.X., Su, S.G., Wu, Z.X., 2009. Nomenclature, diagnosis and origin of High-Magnesian Andesits (HMA) and Magnesian Andesits (MA): A review from petrographic and experimental data. Proceedings of Goldsehmidt Conference Abstracts, Davos, Switzerland, p. A279.
Ding, L., Lai, Q.Z., 2003. New geological evidence of crustal thickening in the Gangdese block prior to the Indo-Asian collision. Chinese Science Bulletin 48, 1604–1610.
Ding, L., Kapp, P., Zhong, D.L., Deng, W.M., 2003. Cenozoic volcanism in Tibet: evidence for a transition from oceanic to continental subduction. Journal of Petrology 44, 1833–1865.
Falloon, T.J., Danyushesky, L.V., 2000. Melting of refractory mantle at 1.5, 2 and 2.5 GPa under anhydrous and H2O-undersaturated conditions: implications for the petrogenesis of high-Ca boninites and the influence of subduction components on mantle melting. Journal of Petrology 41, 257–283.
Gao, S., Rudnick, R.L., Yuan, H.L., Liu, X.M., Liu, Y.S., Xu, W.L., Ling, W.L., Ayers, J., Wang, X.C., Wang, Q.H., 2004. Recycling lower continental crust in the North China craton. Nature 432, 892–897.
Geng, Q.R., Pan, G.T., Wang, L.Q., Peng, Z.M., Zhang, Z., 2011. Tethyan evolution and metallogenic geological background of the Bangong Co-Nujiang belt and the Qiangtang massif in Tibet. Geological Bulletin of China 30, 1261–1274 (in Chinese with English abstract).
Griffin, W.L., Wang, X., Jackson, S.E., Pearson, N.J., O'Reilly, S.Y., Xu, X.S., Zhou, X.M., 2002. Zircon chemistry and magma mixing, SE China: in-situ analysis of Hf isotopes, Tonglu and Pingtan igneous complexes. Lithos 61, 237–269.
Guo, F., Nakamuru, E., Fan, W.M., Kobayoshi, K., Li, C.W., 2007. Generation of Palaeocene adakitic andesites by magma mixing; Yanji Area, NE China. Journal of Petrology 48, 661–692.
Guynn, J.H., Kapp, P., Pullen, A., Heizler, M., Gehrels, G., Ding, L., 2006. Tibetan basement rocks near Amdo reveal "missing" Mesozoic tectonism along the Bangong suture, central Tibet. Geology 34, 505–508.
Guynn, J.H., Tropper, P., Kapp, P., Gehrels, G.E., 2013. Metamorphism of the Amdo metamorphic complex, Tibet: implications for the Jurassic tectonic evolution of the Bangong suture zone. Journal of Metamorphic Geology 31, 705–727.
Harrison, T.M., Copeland, P., Kidd, W.S.F., Yin, A., 1992. Raising tibet. Science 255, 1663–1670.
Hawkesworth, C.J., Kemp, A.I.S., 2006. Evolution of the continental crust. Nature 443, 811–817.
Jahn, B.M., 2004. The Central Asian Orogenic Belt and growth of the continental crust in the Phanerozoic. Geological Society, London, Special Publications 226, 73–100.
Ji, W.Q., Wu, F.Y., Chung, S.L., Li, J.X., Liu, C.Z., 2009. Zircon U–Pb geochronology and Hf isotopic constraints on petrogenesis of the Gangdese batholith, southern Tibet. Chemical Geology 262, 229–245.
Kamei, A., Owada, M., Nagao, T., Shiraki, K., 2004. High-Mg diorites derived from sanukitic HMA magmas, Kyushu Island, southwest Japan arc: evidence from clinopyroxene and whole rock compositions. Lithos 75, 359–371.
Kapp, P., Murphy, M.A., Yin, A., Harrison, T.M., Ding, L., Guo, J.H., 2003. Mesozoic and Cenozoic tectonic evolution of the Shiquanhe area of western Tibet. Tectonics 22.
Kapp, P., Yin, A., Harrison, T.M., Ding, L., 2005. Cretaceous-Tertiary shortening, basin development, and volcanism in central Tibet. Geological Society of America Bulletin 117, 865–878.
Kelemen, P.B., Hanghøj, K., Greene, A.R., 2014. 4.21 — one view of the geochemistry of subduction-related magmatic arcs, with an emphasis on primitive andesite and lower crust. In: Turekian, H.D.H.K. (Ed.), Treatise on Geochemistry, Second edition Elsevier, Oxford, pp. 749–806.
Kemp, A.I.S., Hawkesworth, C.J., Foster, G.L., Paterson, B.A., Woodhead, J.D., Hergt, J.M., Gray, C.M., Whitehouse, M.J., 2007. Magmatic and crustal differentiation history of granitic rocks from Hf–O isotopes in zircon. Science 315, 980–983.
Kessel, R., Schmidt, M.W., Ulmer, P., Pettke, T., 2005. Trace element signature of subduction-zone fluids, melts and supercritical liquids at 120–180 km depth. Nature 437, 724–727.
Kind, R., Ni, J., Zhao, W.J., Wu, J.X., Yuan, X.H., Zhao, L.S., Sandvol, E., Reese, C., Nabelek, J., Hearn, T., 1996. Evidence from earthquake data for a partially molten crustal layer in southern Tibet. Science 274, 1692–1694.
Kröner, A., Kovach, V., Belousova, E., Hegner, E., Armstrong, R., Dolgopolova, A., Seltmann, R., Alexeiev, D., Hoffmann, J., Wong, J., 2014. Reassessment of continental growth during the accretionary history of the Central Asian Orogenic Belt. Gondwana Research 25, 103–125.

Lee, C.T.A., Morton, D.M., Kistler, R.W., Baird, A.K., 2007. Petrology and tectonics of Phanerozoic continent formation: from island arcs to accretion and continental arc magmatism. Earth and Planetary Science Letters 263, 370–387.
Li, X.H., Liu, D.Y., Sun, M., LI, W.X., Liang, X.R., Liu, Y., 2004. Precise Sm–Nd and U–Pb isotopic dating of the supergiant Shizhuyuan polymetallic deposit and its host granite, SE China. Geological Magazine 141, 225–231.
Li, C., Zhai, Q.G., Dong, Y.S., Huang, X.P., 2006. Discovery of eclogite and its geological significance in Qiangtang area, central Tibet. Chinese Science Bulletin 51, 1095–1100 (in Chinese with English abstract).
Li, J.X., Qin, K.Z., Li, G.M., Xiao, B., Zhao, J.X., Chen, L., 2011. Magmatic–hydrothermal evolution of the Cretaceous Duolong gold-rich porphyry copper deposit in the Bangongco metallogenic belt, Tibet: evidence from U–Pb and 40 Ar/39 Ar geochronology. Journal of Asian Earth Sciences 41, 525–536.
Li, J.X., Qin, K.Z., Li, G.M., Xiao, B., Zhao, J.X., Cao, M.J., Chen, L., 2013. Petrogenesis of ore-bearing porphyries from the Duolong porphyry Cu–Au deposit, central Tibet: evidence from U–Pb geochronology, petrochemistry and Sr–Nd–Hf–O isotope characteristics. Lithos 160, 216–227.
Li, J.X., Qin, K.Z., Li, G.M., Richards, J.P., Zhao, J.X., Cao, M.J., 2014a. Geochronology, geochemistry, and zircon Hf isotopic compositions of Mesozoic intermediate–felsic intrusions in central Tibet: petrogenetic and tectonic implications. Lithos 198, 77–91.
Li, S.M., Zhu, D.C., Wang, Q., Zhao, Z.D., Sui, Q.L., Liu, S.A., Liu, D., Mo, X.X., 2014b. Northward subduction of Bangong–Nujiang Tethys: insight from Late Jurassic intrusive rocks from Bangong Tso in western Tibet. Lithos 205, 284–297.
Liu, Y.S., Gao, S., Hu, Z.C., Gao, C.G., Zong, K.Q., Wang, D.B., 2009. Continental and oceanic crust recycling-induced melt–peridotite interactions in the Trans-North China Orogen: U–Pb dating, Hf isotopes and trace elements in zircons from mantle xenoliths. Journal of Petrology egp082.
Liu, S., Hu, R.Z., Gao, S., Feng, C.X., Coulson, I.M., Feng, G.Y., Qi, Y.Q., Yang, Y.H., Yang, C.G., Tang, L., 2012. U–Pb zircon age, geochemical and Sr–Nd isotopic data as constraints on the petrogenesis and emplacement time of andesites from Gerze, southern Qiangtang Block, northern Tibet. Journal of Asian Earth Sciences 45, 150–161.
Liu, D.L., Huang, Q.S., Fan, S.Q., Zhang, L.Y., Shi, R.D., Ding, L., 2014. Subduction of the Bangong–Nujiang Ocean: constraints from granites in the Bangong Co area, Tibet. Geological Journal 49, 188–206.
Ludwig, K.R., 2003. User's manual for Isoplot 3.00: a geochronological toolkit for Microsoft Excel. Kenneth R. Ludwig.
Ma, L., Wang, Q., Wyman, D.A., Jiang, Z.Q., Yang, J.H., Li, Q.L., Gou, G.N., Guo, H.F., 2013a. Late Cretaceous crustal growth in the Gangdese area, southern Tibet: petrological and Sr–Nd–Hf–O isotopic evidence from Zhengga diorite–gabbro. Chemical Geology 349, 54–70.
Ma, L., Wang, Q., Wyman, D.A., Li, Z.X., Jiang, Z.Q., Yang, J.H., Gou, G.N., Guo, H.F., 2013b. Late Cretaceous (100–89 Ma) magnesian charnockites with adakitic affinities in the Milin area, eastern Gangdese: partial melting of subducted oceanic crust and implications for crustal growth in southern Tibet. Lithos 175, 315–332.
Macpherson, C.G., Dreher, S.T., Thirlwall, M.F., 2006. Adakites without slab melting: high pressure differentiation of island arc magma, Mindanao, the Philippines. Earth and Planetary Science Letters 243, 581–593.
Mann, U., Schmidt, M.W., 2015. Melting of pelitic sediments at subarc depths: 1. Flux vs. fluid-absent melting and a parameterization of melt productivity. Chemical Geology 404, 150–167.
Marschall, H.R., Schumacher, J.C., 2012. Arc magmas sourced from melange diapirs in subduction zones. Nature Geoscience 5, 862–867.
McCarron, J.J., Smellie, J.L., 1998. Tectonic implications of fore-arc magmatism and generation of high-magnesian andesites: Alexander Island, Antarctica. Journal of the Geological Society 155, 269–280.
McCulloch, M.T., Chappell, B.W., 1982. Nd isotopic characteristics of S-and I-type granites. Earth and Planetary Science Letters 58, 51–64.
Middlemost, E.A.K., 1994. Naming materials in the magma/igneous rock system. Earth-Science Reviews 37, 215–224.
Mišković, A., Schaltegger, U., 2009. Crustal growth along a non-collisional cratonic margin: a Lu–Hf isotopic survey of the Eastern Cordilleran granitoids of Peru. Earth and Planetary Science Letters 279, 303–315.
Miyashiro, A., 1974. Volcanic rock series in island arcs and active continental margins. American Journal of Science 274, 321–355.
Mo, X.X., Hou, Z.Q., Niu, Y.L., Dong, G.C., Qu, X.M., Zhao, Z.D., Yang, Z.M., 2007. Mantle contributions to crustal thickening during continental collision: evidence from Cenozoic igneous rocks in southern Tibet. Lithos 96, 225–242.
Mo, X.X., Niu, Y.L., Dong, G.C., Zhao, Z.D., Hou, Z.Q., Zhou, S., Ke, S., 2008. Contribution of syncollisional felsic magmatism to continental crust growth: a case study of the Paleogene Linzizong volcanic succession in southern Tibet. Chemical Geology 250, 49–67.
Moyen, J.F., 2009. High Sr/Y and La/Yb ratios: the meaning of the "adakitic signature". Lithos 112, 556–574.
Niu, Y.L., 2009. Mantle input to the crust in southern Gangdese, Tibet, during the Cenozoic: zircon Hf isotopic evidence. Journal of Earth Science 20, 241–249.
Niu, Y.L., Batiza, R., 1997. Trace element evidence from seamounts for recycled oceanic crust in the Eastern Pacific mantle. Earth and Planetary Science Letters 148, 471–483.
Pan, G.T., Ding, J., Yao, D.S., Wang, L.Q., 2004. Guidebook of 1: 1,500,000 Geologic Map of the Qinghai–Xizang (Tibet) Plateau and Adjacent Areas. Chengdu Cartographic Publishing House, Chengdu Cartographic Publishing House.
Pan, G.T., Mo, X.X., Hou, Z.Q., Zhu, D.C., Wang, L.Q., Li, G.M., Zhao, Z.D., Geng, Q.R., Liao, Z.L., 2006. Spatial–temporal framework of the Gangdese Orogenic Belt and its evolution. Acta Petrologica Sinica 22, 521–533 (in Chinese with English abstract).
Plank, T., 2005. Constraints from thorium/lanthanum on sediment recycling at subduction zones and the evolution of the continents. Journal of Petrology 46, 921–944.
Plank, T., Langmuir, C.H., 1998. The chemical composition of subducting sediment and its consequences for the crust and mantle. Chemical Geology 145, 325–394.
Qian, Q., Hermann, J., 2010. Formation of high-Mg diorites through assimilation of peridotite by monzodiorite magma at crustal depths. Journal of Petrology 51, 1381–1416.
Qiu, R.Z., Deng, J.F., Zhou, S., Li, T.D., Xiao, Q.H., Guo, T.Y., Cai, Z.Y., Li, G.L., Huang, G.C., Meng, X.J., 2005. Ophiolite types in Western Qinghai-Tibetan Plateau, evidences from petrology and geochemistry. Earth Science Frontiers 12, 277–291 (in Chinese with English abstract).
Qu, X.M., Wang, R.J., Xin, H.B., Zhao, Y.Y., Fan, X.T., 2009. Geochronology and geochemistry of igneous rocks related to the subduction of the Tethys oceanic plate along the Bangong Lake arc zone, the western Tibetan Plateau. Geochimica 38, 523–535 (in Chinese with English abstract).
Rapp, R.P., Shimizu, N., Norman, M.D., Applegate, G.S., 1999. Reaction between slab-derived melts and peridotite in the mantle wedge: experimental constraints at 3.8 GPa. Chemical Geology 160, 335–356.
Rudnick, R.L., 1995. Making continental crust. Nature 378, 571–577.
Samson, S.D., McClelland, W.C., Patchett, P.J., Gehrels, G.E., Anderson, R.G., 1989. Evidence from neodymium isotopes for mantle contributions to Phanerozoic crustal genesis in the Canadian Cordillera. Nature 337, 705–709.
Sengör, A.M.C., Natal'In, B.A., Burtman, V.S., 1993. Evolution of the Altaid tectonic collage and Palaeozoic crustal growth in Eurasia. Nature 364, 299–307.
Shi, R.D., Yang, J.S., Xu, Z.Q., Qi, X.X., 2004. Discovery of the boninite series volcanic rocks in the Bangong Lake ophiolite mélange, western Tibet, and its tectonic implications. Chinese Science Bulletin 49, 1272–1278.
Shimoda, G., Tatsumi, Y., Nohda, S., Ishizaka, K., Jahn, B.M., 1998. Setouchi high-Mg andesites revisited: geochemical evidence for melting of subducting sediments. Earth and Planetary Science Letters 160, 479–492.
Streck, M.J., Leeman, W.P., Chesley, J., 2007. High-magnesian andesite from Mount Shasta: a product of magma mixing and contamination, not a primitive mantle melt. Geology 35, 351–354.
Sui, Q.L., Wang, Q., Zhu, D.C., Zhao, Z.D., Chen, Y., Santosh, M., Hu, Z.C., Yuan, H.L., Mo, X.X., 2013. Compositional diversity of ca. 110 Ma magmatism in the northern Lhasa Terrane, Tibet: implications for the magmatic origin and crustal growth in a continent–continent collision zone. Lithos 168, 144–159.
Sun, S.S., McDonough, W.F., 1989. Chemical and isotopic systematics of oceanic basalts: implications for mantle composition and processes. Geological Society, London, Special Publications 42, 313–345.
Tang, G.J., Wang, Q., Wyman, D.A., Li, Z.X., Zhao, Z.H., Jia, X.H., Jiang, Z.Q., 2010. Ridge subduction and crustal growth in the Central Asian Orogenic Belt: evidence from Late Carboniferous adakites and high-Mg diorites in the western Junggar region, northern Xinjiang (west China). Chemical Geology 277, 281–300.
Tatsumi, Y., 2001. Geochemical modeling of partial melting of subducting sediments and subsequent melt–mantle interaction: generation of high-Mg andesites in the Setouchi volcanic belt, southwest Japan. Geology 29, 323–326.
Tatsumi, Y., Hanyu, T., 2003. Geochemical modeling of dehydration and partial melting of subducting lithosphere: toward a comprehensive understanding of high-Mg andesite formation in the Setouchi volcanic belt, SW Japan. Geochemistry, Geophysics, Geosystems 4.
Taylor, S.R., McLennan, S.M., 1995. The geochemical evolution of the continental crust. Reviews of Geophysics 33, 241–265.
Taylor, R.N., Nesbitt, R.W., Vidal, P., Harmon, R.S., Auvray, B., Croudace, I.W., 1994. Mineralogy, chemistry, and genesis of the boninite series volcanics, Chichijima, Bonin Islands, Japan. Journal of Petrology 35, 577–617.
Vervoort, J.D., Patchett, P.J., Blichert-Toft, J., Albarède, F., 1999. Relationships between Lu–Hf and Sm–Nd isotopic systems in the global sedimentary system. Earth and Planetary Science Letters 168, 79–99.
Wang, Q., McDermott, F., Xu, J.F., Bellon, H., Zhu, Y.t., 2005. Cenozoic K-rich adakitic volcanic rocks in the Hohxil area, northern Tibet: lower-crustal melting in an intracontinental setting. Geology 33, 465–468.
Wang, Q., Wyman, D.A., Xu, J.F., Zhao, Z.H., Jian, P., Xiong, X.L., Bao, Z.W., Li, C.F., Bai, Z.H., 2006a. Petrogenesis of Cretaceous adakitic and shoshonitic igneous rocks in the Luzong area, Anhui Province (eastern China): implications for geodynamics and Cu–Au mineralization. Lithos 89, 424–446.
Wang, Q., Xu, J.F., Jian, P., Bao, Z.W., Zhao, Z.H., Li, C.F., Xiong, X.L., Ma, J.L., 2006b. Petrogenesis of adakitic porphyries in an extensional tectonic setting, Dexing, South China: implications for the genesis of porphyry copper mineralization. Journal of Petrology 47, 119–144.
Wang, Q., Wyman, D.A., Zhao, Z.H., Xu, J.F., Bai, Z.H., Xiong, X.L., Dai, T.M., Li, C.F., Chu, Z.Y., 2007. Petrogenesis of Carboniferous adakites and Nb-enriched arc basalts in the Alataw area, northern Tianshan Range (western China): implications for Phanerozoic crustal growth in the Central Asia orogenic belt. Chemical Geology 236, 42–64.
Wang, Q., Wyman, D.A., Xu, J.F., Dong, Y.H., Vasconcelos, P.M., Pearson, N., Wan, Y.S., Dong, H., Li, C.F., Yu, Y.S., 2008a. Eocene melting of subducting continental crust and early uplifting of central Tibet: evidence from central-western Qiangtang high-K calc-alkaline andesites, dacites and rhyolites. Earth and Planetary Science Letters 272, 158–171.
Wang, Q., Wyman, D.A., Xu, J.F., Wan, Y.S., Li, C.F., Zi, F., Jiang, Z.Q., Qiu, H.N., Chu, Z.Y., Zhao, Z.H., 2008b. Triassic Nb-enriched basalts, magnesian andesites, and adakites of the Qiangtang terrane (Central Tibet): evidence for metasomatism by slab-derived melts in the mantle wedge. Contributions to Mineralogy and Petrology 155, 473–490.
Wang, Q., Li, Z.X., Chung, S.L., Wyman, D.A., Sun, Y.L., Zhao, Z.H., Zhu, Y.T., Qiu, H.N., 2011. Late Triassic high-Mg andesite/dacite suites from northern Hohxil, North Tibet: geochronology, geochemical characteristics, petrogenetic processes and tectonic implications. Lithos 126, 54–67.
Wang, Q., Zhu, D.C., Zhao, Z.D., Liu, S.A., Chung, S.L., Li, S.M., Liu, D., Dai, J.G., Wang, L.Q., Mo, X.X., 2014. Origin of the ca. 90 Ma magnesia-rich volcanic rocks in SE Nyima, central Tibet: products of lithospheric delamination beneath the Lhasa–Qiangtang collision zone. Lithos 198, 24–37.

Wu, F.Y., Yang, Y.H., Xie, L.W., Yang, J.H., Xu, P., 2006. Hf isotopic compositions of the standard zircons and baddeleyites used in U–Pb geochronology. Chemical Geology 234, 105–126.
Xie, L.W., Zhang, Y.B., Zhang, H.H., Sun, J.F., Wu, F.Y., 2008. In situ simultaneous determination of trace elements, U–Pb and Lu–Hf isotopes in zircon and baddeleyite. Chinese Science Bulletin 53, 1565–1573.
Xu, J.F., Shinjo, R., Defant, M.J., Wang, Q., Rapp, R.P., 2002. Origin of Mesozoic adakitic intrusive rocks in the Ningzhen area of east China: partial melting of delaminated lower continental crust? Geology 30, 1111–1114.
Xu, M.J., Li, C., Zhang, X.Z., Wu, Y.W., 2014. Nature and evolution of the Neo-Tethys in central Tibet: synthesis of ophiolitic petrology, geochemistry, and geochronology. International Geology Review 56, 1072–1096.
Yang, J.H., Wu, F.Y., Wilde, S.A., Xie, L.W., Yang, Y.H., Liu, X.M., 2007. Tracing magma mixing in granite genesis: in situ U–Pb dating and Hf-isotope analysis of zircons. Contributions to Mineralogy and Petrology 153, 177–190.
Yin, A., Harrison, T.M., 2000. Geologic evolution of the Himalayan-Tibetan orogen. Annual Review of Earth and Planetary Sciences 28, 211–280.
Zhang, Y.X., 2007. Tectonic evolution of the middle-western Bangong–Nujiang suture, Tibet. Unpublished Doctoral thesis, Guangzhou Institute of Geochemistry, Chinese Academy of Sciences.
Zhang, K.J., Zhang, Y.X., Tang, X.C., Xia, B., 2012a. Late Mesozoic tectonic evolution and growth of the Tibetan plateau prior to the Indo-Asian collision. Earth-Science Reviews 114, 236–249.
Zhang, Z.M., Dong, X., Liu, F., Lin, Y.H., Yan, R., Santosh, M., 2012b. Tectonic evolution of the Amdo Terrane, Central Tibet: petrochemistry and zircon U–Pb geochronology. Journal of Geology 120, 431–451.
Zhang, K.J., Xia, B., Zhang, Y.X., Liu, W.L., Zeng, L., Li, J.F., Xu, L.F., 2014a. Central Tibetan Meso-Tethyan oceanic plateau. Lithos 210, 278–288.
Zhang, X.R., Shi, R.D., Huang, Q.S., Liu, D.L., Gong, X.H., Chen, S.S., Wu, K., Yi, G.D., Sun, Y.L., Ding, L., 2014b. Early Jurassic high-pressure metamorphism of the Amdo terrane, Tibet: constraints from zircon U–Pb geochronology of mafic granulites. Gondwana Research 26, 975–985.
Zhang, Z.M., Dong, X., Xiang, H., He, Z.Y., Liou, J.G., 2014c. Metagabbros of the Gangdese arc root, south Tibet: implications for the growth of continental crust. Geochimica et Cosmochimica Acta 143, 268–284.
Zhu, D.C., Pan, G.T., Mo, X.X., Wang, L.Q., Liao, Z.L., Zhao, Z.D., Dong, G.C., Zhou, C.Y., 2006a. Late Jurassic–Early Cretaceous geodynamic setting in middle-northern Gangdese; new insights from volcanic rocks. Acta Petrologica Sinica 22, 534–546 (in Chinese with English abstract).
Zhu, D.C., Pan, G.T., Mo, X.X., Wang, L.Q., Zhao, Z.D., Liao, Z.L., Geng, Q.R., Dong, G.C., 2006b. Identification for the Mesozoic OIB-type basalts in central Qinghai-Tibetan Plateau: geochronology, geochemistry and their tectonic setting. Acta Geologica Sinica 80, 1312–1328 (in Chinese with English abstract).
Zhu, D.C., Mo, X.X., Niu, Y.L., Zhao, Z.D., Wang, L.Q., Liu, Y.S., Wu, F.Y., 2009. Geochemical investigation of Early Cretaceous igneous rocks along an east–west traverse throughout the central Lhasa Terrane, Tibet. Chemical Geology 268, 298–312.
Zhu, D.C., Zhao, Z.D., Niu, Y.L., Mo, X.X., Chung, S.L., Hou, Z.Q., Wang, L.Q., Wu, F.Y., 2011. The Lhasa Terrane: record of a microcontinent and its histories of drift and growth. Earth and Planetary Science Letters 301, 241–255.
Zhu, D.C., Zhao, Z.D., Niu, Y.L., Dilek, Y., Hou, Z.Q., Mo, X.X., 2013. The origin and pre-Cenozoic evolution of the Tibetan Plateau. Gondwana Research 23, 1429–1454.
Zhu, D.C., Li, S.M., Cawood, P.A., Wang, Q., Zhao, Z.D., Liu, S.A., Wang, L.Q., 2016. Assembly of the Lhasa and Qiangtang terranes in central Tibet by divergent double subduction. Lithos 245, 7–17.